*

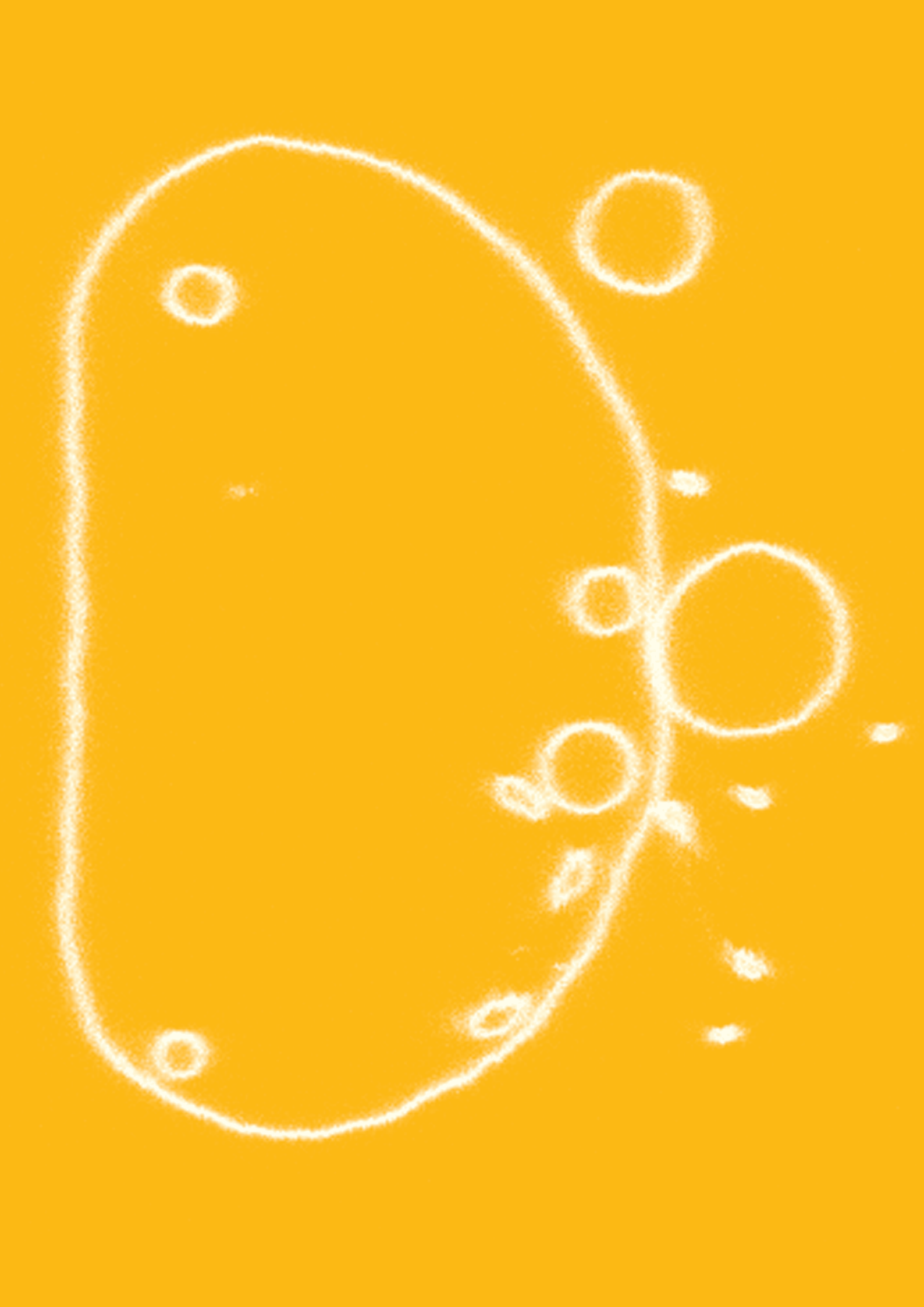

→ Polymers and Proteins
→ Molecular Motors
→ Membranes and Vesicles
→ Networks in Bio-Systems

THEORY & BIO-SYSTEMS

Research in the Department of Theory & Bio-Systems

There's plenty of room at the bottom
Richard Feynman

The researchers and graduate students of the Department of Theory and Bio-Systems form one experimental and several theoretical research teams. Each of these teams consists of the team leader and several students. The team leaders are:

- *Rumiana Dimova* (experiment, membranes and vesicles).
- *Thomas Gruhn* (theory, membranes and vesicles; until 2007);
- *Jan Kierfeld* (theory, polymers and filaments; until 2007);
- *Volker Knecht* (theory; proteins and membranes).
- *Christian Seidel* (theory, polymers and poly-electrolytes);
- *Thomas Weikl* (theory, proteins and membranes).

The Theory and Bio-Systems Department is responsible for the International Max Planck Research School on 'Biomimetic Systems'. Until the end of 2008, the department also coordinated the European Early Stage Training Network about the same topic and the European Research Network on `Active Biomimetic Systems'. The graduate programs are managed by *Angelo Valleriani*.

In the following three subsections, the research within the Theory and Bio-Systems Department is described in terms of the underlying molecular systems, the cooperative phenomena found in these systems, and the methods used to study them.

Systems

Our research is focused on bio-systems, which represents an abbreviation for 'biomimetic and biological systems'. If one looks at these systems bottom-up, i.e., from small to large length scales, one encounters a hierarchy of such systems including:

- polymers and proteins,
- molecular motors,
- rods and filaments,
- membranes and vesicles, and
- networks in bio-systems.

When these systems are approached top-down, i.e., from larger to smaller scales, one encounters the problem of restricted geometries or confining walls and interfaces. In general, interfaces may be used to suspend and organize smaller bio-systems in order to make them accessible to systematic studies.

Phenomena

During the last two years, specific phenomena addressed in the area of polymers and proteins included the conformation of peptides at interfaces, the process of protein folding, and dense brushes of polyelectrolytes. As far as motor proteins or molecular motors are concerned, we studied the chemomechanical coupling of single motors and the cooperative transport of cargo particles by several such motors. When these motors belong to two different species, they perform a stochastic tug-of-war as shown in **Fig. 1**.

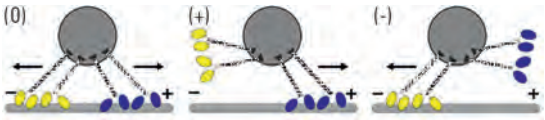

Fig. 1: Tug-of-war between 2 plus (blue) and 2 minus (yellow) motors pulling on the same cargo particle (gray). For configuration (0), the motors block each other so that the cargo does not move. For configuration (+) and (-), the cargo exhibits fast plus and minus motion, respectively.

One particularly intriguing aspect of filaments is the coupling of filament growth to active processes. One example is provided by actin polymerization coupled to ATP hydrolysis. In order to elucidate this process, we introduced a new theoretical model for cooperative ATP cleavage and Pi release as shown in **Fig. 2**.

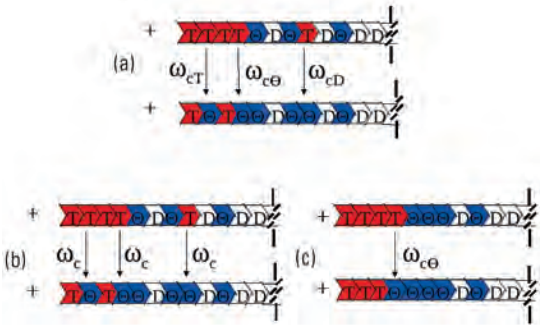

Fig. 2: Actin filaments consisting of three different types of protomers denoted T, Θ and D: (a) Cooperative ATP cleavage depending on the local neighborhood of the T protomer within the filament; (b) Random ATP cleavage and (c) Vectorial ATP cleavage.

In the research field of membranes and vesicles, we have improved our theoretical models for membrane fusion and membrane adhesion. A timely topic is the adhesion of multicomponent membranes to solid substrates as shown in **Fig. 3.** In addition, the deformation of lipid vesicles by alternating electric fields has been studied experimentally as a function of ion conductivities and field frequency, see **Fig. 4**.

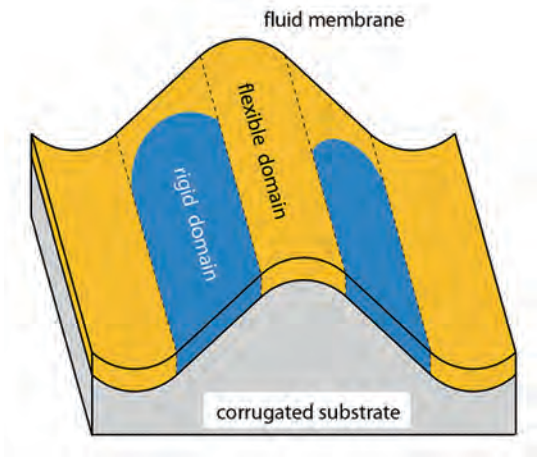

Fig. 3: Fluid membrane on a corrugated, solid substrate with two types of domains (blue and yellow) that differ in their bending rigidity. The blue domains are more rigid than the yellow one and tend to avoid the curved membrane parts provided the line tension of the domain boundaries is sufficiently small.

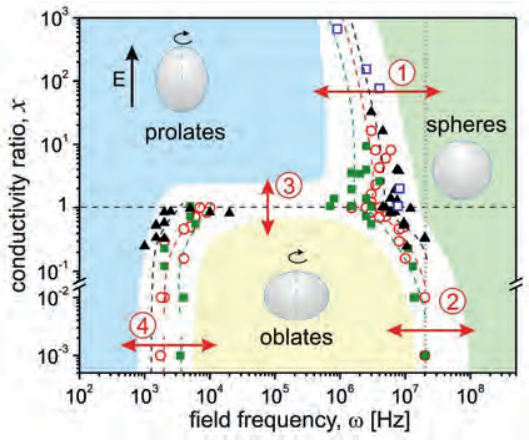

Fig. 4: Morphological diagram for lipid vesicles in alternating electric fields as function of field frequency and conductivity ratio.

Bio-systems are quite complex and exhibit many levels of self-organization. One rather general framework for these systems is provided by network models. During the last two years, we have worked on networks of motor cycles, activity pattern on scale-free networks, and simple neural networks.

Most of the systems and phenomena that have been mentioned in this overview will be covered in more detail on the following pages.

Methods

The conceptual framework for the understanding of these systems and their cooperative behavior is provided by statistical physics which includes thermodynamics, statistical mechanics, and stochastic processes.

The theory of work starts with the definition of a certain model which (i) is amenable to systematic theoretical analysis and (ii) captures the essential features of the real system and its behavior. In general, the challenge is to find a theoretical representation that depends only on experimentally accessible parameters.

The theoretical models are then studied using the analytical tools of theoretical physics and a variety of numerical algorithms. The analytical tools include dimensional analysis, scaling arguments, molecular field or self-consistent theories, perturbation theories, and field-theoretic methods such as renormalization. The numerical methods include the application of mathematical software packages for calculus and algebra as well as special algorithms such as, e.g., the Surface Evolver for the calculation of constant mean curvature surfaces.

Several types of computer simulations are applied and further developed: Molecular Dynamics, Dissipative Particle Dynamics, Brownian Dynamics, and Monte Carlo methods. Molecular Dynamics is used for particle based models of supramolecular assemblies; Dissipative Particle Dynamics is useful in order to extend the Molecular Dynamics studies towards larger systems and longer time scales; Brownian Dynamics and Monte Carlo methods are used in order to simulate even larger mesoscopic systems such as filaments and membranes up to a linear size of hundreds of nanometers.

Experimental work is carried out in our membrane lab which is equipped with calorimetry, optical microscopy, micropipettes, and optical tweezers. This lab is also responsible for the advanced confocal microscope that is available to all departments of the MPI.

Additional information about research in the Theory Department is avalaible at *www.mpikg.mpg.de/th/*

Reinhard Lipowsky
Director of the Department
of Theory & Bio-Systems

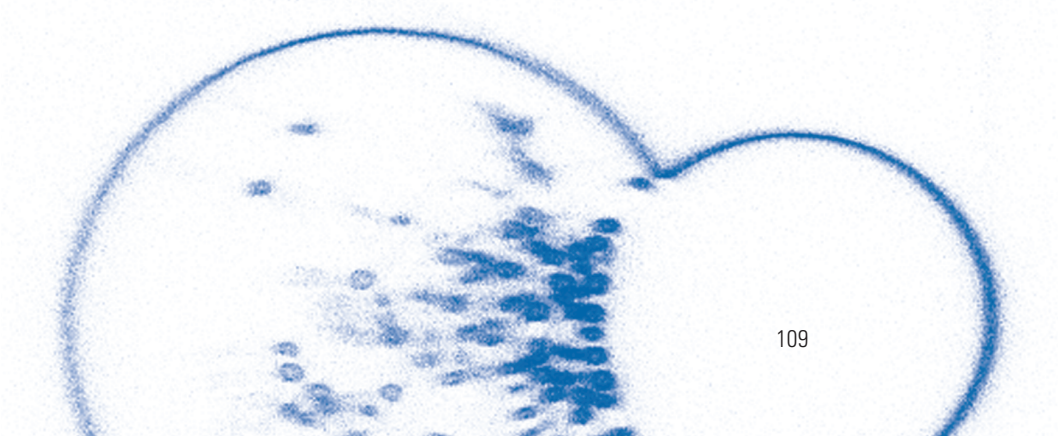

Polypeptides: Amyloid Formers and Molecular Motors

Volker Knecht 06.01.1970
1996: Diploma in physics (University of Kaiserslautern)
Thesis: Computer based renormalization group study of the two-dimensional XY model
1997: Software trainee (TECMATH GmbH, Kaiserslautern)
1998-1999: Software engineer (LMS Durability Technologies GmbH, Kaiserslautern)
2003: PhD, Physics (MPI of biophysical chemistry, Göttingen)
Thesis: Mechanical coupling via the membrane fusion SNARE protein syntaxin 1A: a molecular dynamics study
2003-2005: Postdoc (University of Groningen, the Netherlands)
2005-2006: Postdoc (MPI of Colloids and Interfaces, Potsdam)
Since 2006: Group Leader (MPI of Colloids and Interfaces, Potsdam)

Proteins and polypeptides in general are biopolymers composed of amino acid residues that fold into well-defined structures depending on their amino acid sequence. Folding is crucial for the function of a protein whereas misfolding can cause severe diseases. Our aim is to understand protein function and diseases on the molecular level. The information on the molecular dynamics of polypeptides accessible experimentally is very limited. Therefore we use molecular dynamics computer simulation techniques to model the process by which proteins sample conformational space. Molecular dynamics simulations which are based on iteratively solving Newton's equations of motion to propagate a system in time and semi-empirical force fields to describe interatomic interactions can provide highly detailed information about the properties of proteins in solution or at interfaces. Here, the protein and its solvent environment are described in atomic detail. Currently, we focus on the molecular basis of so-called amyloid diseases and the function of molecular motors.

Amyloid Peptides

Amyloid diseases including Alzheimer's, Creutzfeld-Jakob disease and bovine spongiform encephalopathy (BSE) are associated with the conversion of a protein from a soluble (functional) form into higher order fibrillar aggregates rich in β-structure. The development of specific agents against amyloid diseases requires an understanding of the (mis)folding and aggregation of fibrillogenic proteins on a microscopic level. In collaboration with Gerald Brezesinski's group from the Interfaces department, we study the folding and aggregation of small amyloid peptides in solution, see **Fig. 1**, and at interfaces, see **Fig. 2 [1-4]**. The systems investigated include model peptides containing between 12 and 18 residues, see **Fig. 1(a,b)**, as well as an 11-residue fragment of the amyloid β (Aβ) peptide associated with Alzheimer's disease, Aβ(25-35), see **Fig. 1c**.

Fibrillogenic peptides, typically, are found to form β-hairpin as in **Figs. 1(a,b)** and **2(a)** or coil conformations. As shown in **Fig. 1(b)** (middle), a predominant conformation has been identified for the inner residues of the model amyloid peptide LSFD **[4]**. Knowledge of a predominant conformation may facilitate the design of possible inhibitors of LSFD aggregation as a testing ground for future computational therapeutic approaches against amyloid diseases. In ordered aggregates, β-hairpins are either placed side by side, see **Fig. 1(a)**, or dissolved often leading to extended conformations, see **Figs. 1(c)** and **2(b)**. Some of these dimer conformations might reflect the structure of fibrillar aggregates, see **Fig. 1(a,c)**.

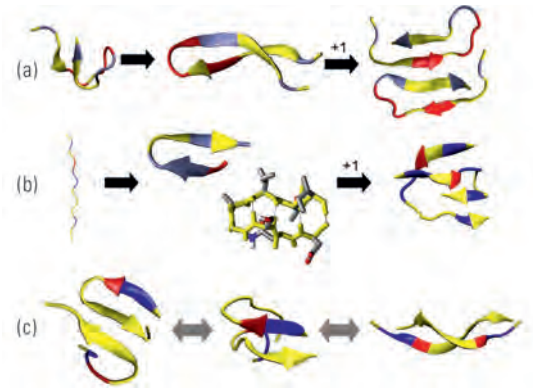

Fig. 1: β-hairpin folding and dimerization of fibrillogenic peptides in solution in molecular dynamics simulations. The model amyloid peptides (a) B18 [1-3] and (b) LSFD [4] as well as (c) the peptide Aβ(25-35) associated with Alzheimer's disease are depicted. Initial and typical backbone configurations during the simulations are shown in ribbon representation. Colors distinguish between hydrophobic (yellow), hydrophilic but neutral (blue), and charged residues (red). In (b), the conformation of the monomer in the folded state is shown as sticks.

For the first time, we have studied reversible β-hairpin peptide folding at an interface, see **Fig. 2(a) [4]**, the formation of side-by-side-hairpin β-sheet dimers **[3]**, see **Fig. 1(a)**, and the conformational distribution of a peptide containing more than ten amino acid residues in dimeric form at equilibrium, see **Fig. 1(c)**, using an explicit solvent model.

The studies are challenging because of the large computational expense of the simulations and the roughness of the free energy landscape underlying folding. Therefore, our initial studies have been restricted to relatively short model peptides. But, using novel methods to enhance the sampling including the coupling of simulations of various copies of the system at different temperatures (replica exchange), we are now investigating larger peptides such the 26-residue peptide Aβ(10-35) in mono- and dimeric form. A non-amyloidogenic peptide of the same size, the (antimicrobial) peptide NK-2, is investigated for comparison.

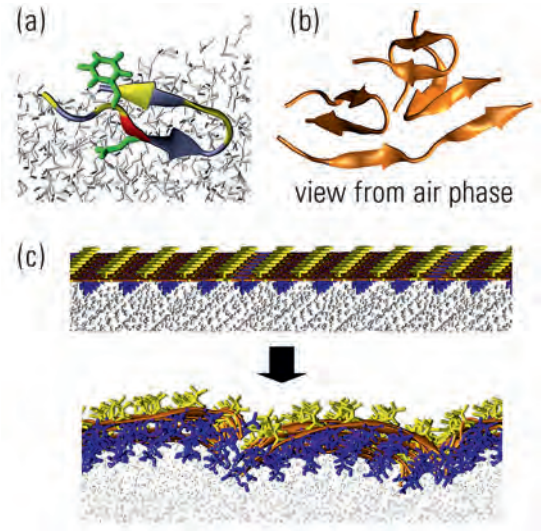

Fig. 2: β-sheet forming peptides at water/vapor interface. An LSFD (a) monomer [4] and (b) tetramer, as well as (c) a crystalline monolayer of the peptide G(VT)$_5$ are depicted. The backbone of the peptides is shown in ribbon representation. In (a), the color code for the peptide backbone is similar to that chosen in Fig. 1, and selected side chains are shown as green sticks. In (c), the side chains of the peptides are displayed as sticks, colors distinguish between valine (yellow) and threonine (blue). In (a) and (c), water molecules are depicted as white sticks.

The synthetic peptide with sequence G(VT)$_5$ synthesized in Hans Börner's lab in the Colloids department has been studied at a water/vapor interface where it forms β-rich crystalline monolayers. Based on data from x-ray scattering and infrared spectroscopy, we modeled an idealized monolayer in which the peptides are extended and form in-register β-sheets over their whole length, see **Fig. 2(c)**, top, and used simulations to refine the structure. We found that the β-strands are strongly bent and that β-sheets are dissolved at the termini as in **Fig. 2(c)**, bottom. When the subphase contains NaCl, both types of ions are strongly adsorbed at the termini of the peptides.

Molecular Motors

The Kinesin molecules represent a large motor-protein family that transports cargoes within a cell by moving on microtubule filaments consisting of α- and β-tubulin dimers coupled to ATP hydrolysis, see **Fig. 3**. Conventional kinesin, henceforth denoted as kinesin, is a homodimer containing two heads by which kinesin binds ATP and walks along microtubules. The molecular details of this process are poorly understood. In order to quantify the energy levels of kinesin in all its nucleotide-binding states, we aim to determine equilibrium constants and activity scales for ATP hydrolysis from quantum-mechanical calculations using a continuum model for the solvent. Test studies to evaluate the accuracy and computational expense of different levels of theory are in progress.

In order to understand the mechanical response of kinesin to the chemical transitions, we are studying the conformational changes of a kinesin monomer in solution and at tubulin during the catalytic cycle using classical molecular dynamics simulations. Structural models based on x-ray crystallography or cryo-electron microscopy are used as input for the simulations. The timescales for each nucleotide state employed here exceed those used in previous studies of the same system by almost two orders of magnitude. We found that the region connecting the head and the adjacent neck region, the neck linker, is highly flexible and, thus, provides a hinge, for all nucleotide states. Currently, we are investigating a kinesin dimer with one of its heads in the ATP state attached to a tubulin dimer, see **Fig. 3(a)**. Within 50 ns of simulation, a large conformational change has occurred, see **Fig. 3(b)**. This study opens the perspective to investigate the mechanical step of kinesin at tubulin, the so-called "power stroke", in full atomic detail.

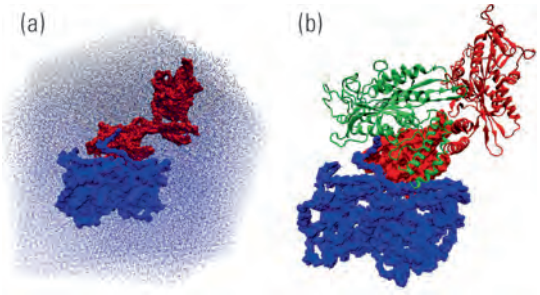

Fig. 3: Modelling the kinesin dimer at tubulin in atomic detail. (a) The system simulated includes a kinesin dimer (red surface) as well as an α-β tubulin dimer ("tubulin", blue surface). The initial configuration of the protein complex has been modelled based on an atomic model of a kinesin monomer at tubulin and a solvated kinesin dimer using rigid body motion and solvated in explicit water (blue dots). (b) Conformation of tubulin (blue) and bound kinesin head (red surface) as well as configuration of the unbound head before (red, ribbons) and after a 50 ns simulation (green).

V. Knecht, N. Awasthi, Y. Chai, C. v. Deuster, M. Kittner, B. Klasczyk, A. Krukau, Y. Smirnowa
vknecht@mpikg.mpg.de

References:

[1] Knecht, V., Möhwald, H., Lipowsky, R.: Conformational diversity of the fibrillogenic fusion peptide B18 in different environments from molecular dynamics simulations, J. Phys. Chem. B **111**, 4161-4170 (2007).
[2] Knecht, V., Lipowsky, R.: Conformational polymorphism of a fibrillogenic fusion peptide in explicit solvent and at an interface, From Computational Biophysics to Systems Biology (CBSB08), edited by Hansmann, U.H.E. et al., NIC Series **40**, Jülich, 109-111 (2008).
[3] Knecht, V., Lipowsky, R.: Folding and formation of side-by-side-hairpin β-sheet dimers by a model amyloid peptide in solution, submitted.
[4] Knecht, V: β-hairpin folding by a model amyloid peptide in solution and at an interface, J. Phys. Chem. B **112**, 9476-9483 (2008).

Protein Folding and Function

Thomas Weikl 01.04.1970
1996: Diploma, Physics
(Freie Universität Berlin)
Thesis: Interactions of rigid membrane inclusions
1999: PhD, Physics
(Max Planck Institute of Colloids and Interfaces, Potsdam)
Thesis: Adhesion of multicomponent membranes
2000-2002: Postdoc
(University of California, San Francisco)
Since 2002: Group Leader
(Max Planck Institute of Colloids and Interfaces, Potsdam)
2008: Habilitation, Physics
(University Potsdam)
Thesis: Transition states and loop-closure principles in protein folding

Transition States in Protein Folding

A current focus of our research is the folding dynamics of small single-domain proteins **[1, 2, 3]**. Many of these proteins are 'two-state folders', i.e. proteins that fold rather directly from the denatured state to the native state, without populating metastable intermediate states. A central question is how to characterize the instable, partially folded conformations of two-state proteins, in particular the rate-limiting transition-state conformations between the denatured and the native state. These partially folded conformations are short-lived and cannot be observed directly in experiments.

However, experimental data from detailed mutational analyses of the folding dynamics provide indirect access to transition states. The interpretation of these data, in particular the reconstruction of transition-state conformations, requires simulation and modeling. The traditional interpretation of the mutational data aims to reconstruct the degree of structure formation of individual residues in the transition state. We have suggested a novel interpretation that aims at degrees of structure formation of cooperative substructures such as α-helices and β-hairpins, which resolves some of the inconsistencies of the traditional interpretation **[4, 5]**.

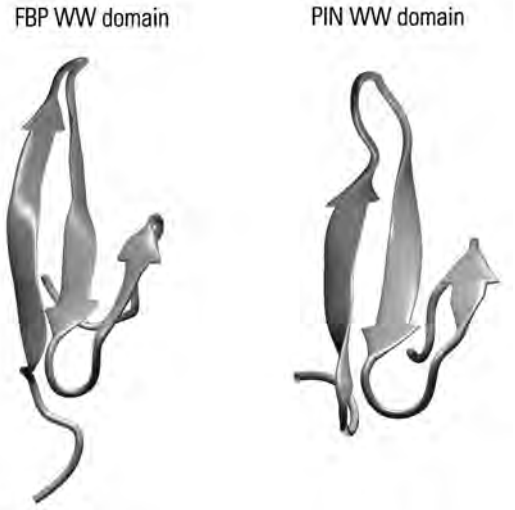

Fig. 1: The structure of WW domains consists of two β-hairpins forming a three-stranded β-sheet. The FBP and PIN WW domain shown here are two-state proteins that fold without experimentally detectable intermediate states.

The smallest β-proteins have just three β-strands. Important representatives of this class of proteins are WW domains, see **Fig. 1**, named after two conserved tryptophan residues, which are represented by the letter W in the single-letter code for amino acids. WW domains are central model systems for understanding β-sheet folding and stability. Molecular Dynamics simulations indicate that the two β-hairpins of three-stranded β-proteins are cooperative substructures.

We have analyzed the detailed mutational data for the FBP and PIN WW domains with a simple four-state model **[5]**. The central assumption of this model is that the transition state of the WW domains consists of two conformations in which either hairpin 1 or hairpin 2 are formed, see **Fig. 2**. The model has two folding routes: On one of the routes, hairpin 1 forms before hairpin 2, and on the other route, after hairpin 2. The folding rate

$$k = c\left(\mathrm{e}^{-G_1/RT} + \mathrm{e}^{-G_2/RT}\right)$$

in this model is sum of the rates for the two folding routes.

Mutations shift the free energies G_1 and G_2 of the transition-state conformations and, thus, shift the folding rate of the protein. By comparing with experimental data for the folding rates of wildtype and mutants of WW domains, we have reconstructed the transition state of these proteins. The structural information obtained from the mutational data is that the transition state ensemble of the FBP WW domain consists to roughly 3/4 of conformation 1 with hairpin 1 formed, and to 1/4 of conformation 2 with hairpin 2 formed. The transition state ensemble of the PIN WW domain consists to roughly 2/3 of conformation 1, and to 1/3 of conformation 2, according to the model.

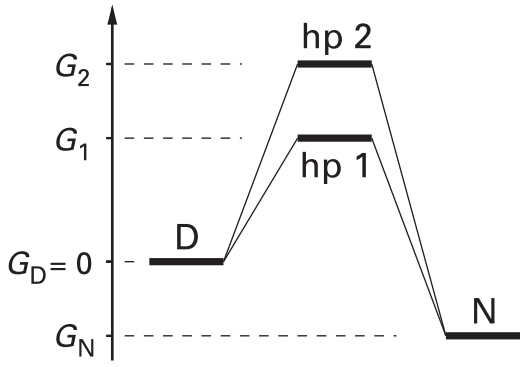

Fig. 2: Simple energy landscape of a four-state model for WW domains. The four states are the denatured state D, the native state N, and two transition-state conformations hp 1 and hp 2 in which either hairpin 1 or hairpin 2 are formed. Here, G_N is the free-energy difference between the native state N and the denatured state D with 'reference free energy' $G_D = 0$, and G_1 and G_2 are the free energy differences between the transition-state conformations and the denatured state.

Conformational Changes During Binding

The sequence of a protein determines the three-dimensional structure, in which it folds. The structure in turn enables the biological function of the protein. During their function, many proteins slightly change and adapt their three-dimensional structures. For example, the binding of a ligand molecule to a protein is often accompanied by conformational changes of the protein. A central question is whether the ligand induces the conformational change (induced-fit), or rather selects and stabilizes a complementary conformation from a pre-existing equilibrium of ground and excited states of the protein (selected-fit).

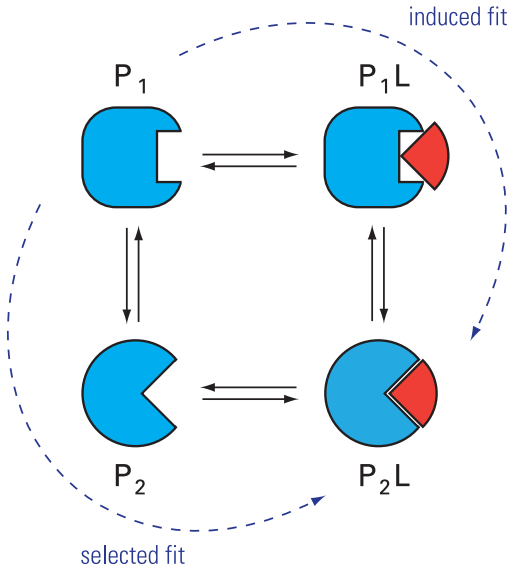

Fig. 3: Simple four-state model of protein-ligand binding. Without the ligand L, the conformation P_1 of the protein is the ground-state conformation, and P_2 is the excited-state conformation. When the ligand is bound, P_2L is the ground state, and P_1L the excited state. On the selected-fit route, the ligand binds the protein in the excited-state conformation P_2, and on the induced-fit binding route, in the ground-state conformation P_1.

We have studied the selected-fit and induced-fit binding kinetics in a four-state model of protein-ligand binding **[6]**. In this model, the protein has two dominant conformations P_1 and P_2 , see **Fig. 3**. The conformation P_1 is the ground-state conformation in the unbound state of the protein, while P_2 is the ground-state conformation in the ligand-bound state. Two routes connect the unbound ground state P_1 and the bound ground state P_2L. On the induced-fit route $P_1 \rightarrow P_1L \rightarrow P_2L$, the protein first binds the ligand in conformation P_1, which causes the transition into conformation P_2. On the selected-fit route $P_1 \rightarrow P_2 \rightarrow P_2L$, the protein binds the ligand in the higher-energy conformation P_2.

We find a characteristic difference between the selected-fit and induced-fit binding kinetics. If the conformational relaxation into the ground state is fast, the selected-fit on-rate depends on the equilibrium constant of the conformations P_1 and P_2 while the selected-fit off-rate is independent of the conformational equilibrium, see **Fig. 4**. The induced-fit on-rate, in contrast, is independent of the conformational equilibrium between P_1L and P_2L, whereas the induced-fit off-rate depends on this equilibrium. Mutations or other perturbations that shift the conformational equilibrium without affecting the shape or free energies of the binding site thus may help to identify whether a protein binds its ligand in a selected-fit or induced-fit mechanism.

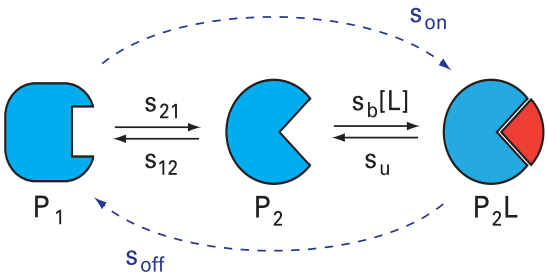

Fig. 4: Binding kinetics along the selected-fit route of the model shown in Fig. 3. Here, s_{21} and s_{12} are the rates for the conformational transitions in the unbound state, s_b is the binding rate of conformation P_2 per mole ligand, and s_u the unbinding rate. Since P_1 is the ground state and P_2 the excited state, the equilibrium constant $K_U = s_{21}/s_{12}$ for the conformational transitions in the unbound state is much smaller than 1. If the conformational transition rate s_{12} into the ground state is much larger than the binding and unbinding rates $s_b[L]$ and s_u, the on-rate along the selected-fit route is approximately $s_{on} \approx K_u\, s_b$, and the off-rate is $s_{off} \approx s_u$.

T. Weikl, C. von Deuster, L. Reich
thomas.weikl@mpikg.mpg.de

References:

[1] Dill, K. A., Ozkan, S. B., Shell, M. S. and Weikl, T. R.: The protein folding problem. Ann. Rev. Biophys. **37**, 289-316 (2008).

[2] Dill, K. A., Ozkan, S. B., Weikl, T. R., Chodera, J. D. and Voelz, V. A.: The protein folding problem: When will it be solved? Curr. Opin. Struct. Biol. **17**, 342-346 (2007).

[3] Weikl, T. R.: Loop-closure principles in protein folding. Arch. Biochem. Biophys. **469**, 67-75 (2008).

[4] Weikl, T. R. and Dill, K. A.: Transition states in protein folding kinetics: The structural interpretation of Φ-values. J. Mol. Biol. **365**, 1578-1586 (2007).

[5] Weikl, T. R.: Transition states in protein folding kinetics: Modeling Φ-values of small β-sheet proteins. Biophys. J. **94**, 929-937 (2008).

[6] Weikl, T. R. and von Deuster, C.: Selected-fit versus induced-fit protein binding: Kinetic differences and mutational analysis. Proteins **75**, 104-110 (2009).

Weak Polyelectrolytes in Poor Solvents

Christian Seidel 07.02.1949
1972: Diploma, Physics (Technical University Dresden) Thesis: in Nuclear Physics
1978: Dr. rer. nat., Polymer Physics (Institute for Polymer Chemistry, Teltow) Thesis: On the calculation of the phonon dispersion of solid polymers, application to polyvinylidenfluoride
1979-83: Research Scientist (Joffe Physico-Technical Institute, Leningrad)
1983-89: Research Scientist (Institute for Polymer Chemistry, Teltow)
1985: Dr. sc. nat., Solid State Theory (Institute for Polymer Chemistry, Teltow) Thesis: Ground states and critical temperatures in quasi-one-dimensional systems
1989-91: Group Leader (Institute for Polymer Chemistry, Teltow)
Since 1992: Group Leader (Max Planck Institute of Colloids and Interfaces, Potsdam)
1994: Habilitation, Theoretical Chemistry (Technical University, Berlin)

Polyelectrolytes (PELs) are macromolecules that contain subgroups with the ability to dissociate charges in polar solvents such as water. PELs have received much attention because of their importance in materials science, soft matter research, and molecular biology. Weak polyelectrolytes such as poly(acrylic acid) dissociate only in a limited pH range. The total charge of the chain is not fixed but can be tuned by changing the pH. The number of charges $N_c = f\,N$ (where N is the number of monomers and f is the degree of ionization) as well as their positions along the polymer are fluctuating quantities. Therefore, weak PELs are also called annealed PELs. The imposed quantity is the chemical potential μ of charges. At high dilution, it equals the solution pH up to a trivial constant and the self energy of the released proton, $\mu = \pm \ln 10\,(\mathrm{pH}-\mathrm{pK}_0) - \lambda_B/\lambda_D$ **[1, 2]**, where pK_0 is the intrinsic dissociation constant of an isolated monomer, λ_B is the Bjerrum length that sets the strength of the Coulomb interaction, $\lambda_D = (8\pi c_s \lambda_B)^{-1/2}$ is the screening length with c_s being the salt concentration, and $\pm$ stands for bases or acids, respectively.

Many polymers are based on a hydrophobic backbone, and charged side groups often determine the solubility of PELs in water. The competition between the attractive monomer-monomer interaction due to a poor solubility of the backbone and the repulsive Coulomb interaction between the polymer charges gives rise to rather complex phase behavior of PELs in poor solvents. In the case of weak or annealed PELs in a poor solvent, the extra charge degree of freedom can have a strong effect: The chains undergo a first-order phase transition between weakly charged globules and strongly charged stretched chains **[1, 3]**. Note that the solvent quality is measured by the distance from the Θ point, $\tau = 1 - T/\Theta$. For a sufficiently poor solvent, $\tau > \tau^* \sim (u^3 N)^{-1/5}$, where $u = \lambda_B/b$ is a dimensionless interaction strength with b being the monomer size, the behavior of the polymer is dominated by this transition. However, if the system is close the Θ point, the discontinuous phase transition is suppressed and intermediate structures such as pearl necklaces can be stable **[4, 5]**.

Although the fundamental behavior of annealed PELs is determined by solvent quality and solution pH, we have demonstrated by means of computer simulations that some fine tuning of dissociation and structure can be enforced by changing the screening length **[6]**. **Fig. 1** shows the size of the polyelectrolyte in the rather-poor-solvent regime, $\tau > \tau^*$, as a function of screening length λ_D. Simulation data are taken at the maximum charge chemical potential μ at which the polyelectrolyte exhibits the transition to an almost uncharged globule. To illustrate the different configurations typical simulation snapshots are added. Hence, for constant solvent quality, interaction strength and solution pH, there is an alternative route to switch the configuration of annealed PELs by changing the ion strength of the solution. In other words, the solution pH at which an annealed PEL undergoes the discontinuous conformational transition can be adjusted by changing the concentration of salt.

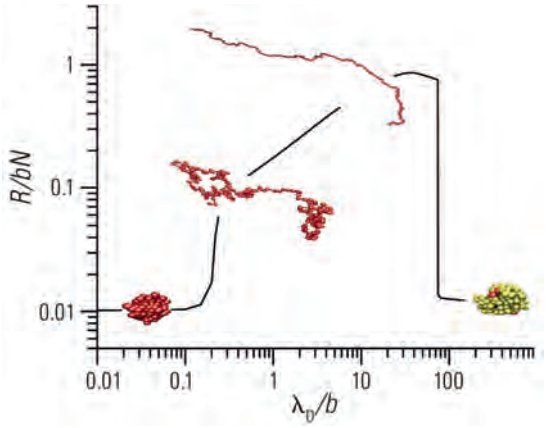

Fig.1: Rather-poor-solvent regime: Mean-square end-to-end-distance R versus screening length λ_D together with typical simulation snapshots. Charged monomers are colored red and uncharged monomers are colored yellow.

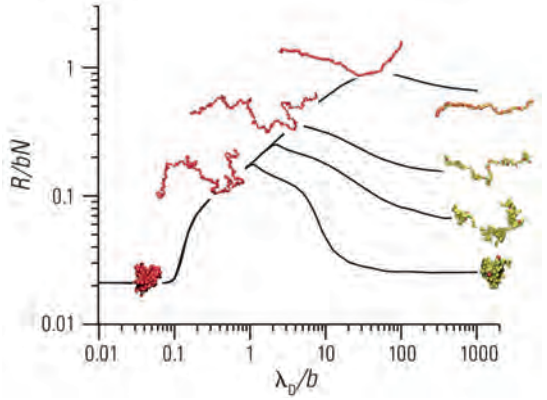

Fig. 2 Close-to-Θ-point regime: Mean-square end-to-end-distance R versus screening length λ_D at growing pH (curves from bottom to top) together with typical simulation snapshots (coloring as in Fig. 1).

In the scaling region $0.3 < \lambda_D/b < 10$, a detailed analysis shows that the polyelectrolyte behaves as a (semi-) flexible chain with persistence length $l_e \sim b(\lambda_D/b)^2$. Using the model of a flexible chain built by cylindrical monomers of length $l_e << Nb$ and diameter λ_D we find good agreement with previous theoretical predictions **[6]**. For larger screening lengths, because of the competition between growing stiffening on large length scales due to the polyelectrolyte effect on the one hand, and increasing wiggling on short length scales due to the reduced dissociation on the other hand, the end-to-end distance R exhibits an unusual non-monotonic behavior with growing λ_D.

In **Fig. 2**, we plot the same quantity as in Fig. 1, but here in the close-to-Θ-point regime, $\tau < \tau^*$. The striking difference is the absence of discrete transitions. Depending on the solution pH, continuous crossover behavior between various conformations is observed. Weakly charged pearl necklace structures first described by Dobrynin, Rubinstein and Obukhov (DRO) **[7]** appear at only low pH if the low ionization regime is reached. The population of different pearl necklace configurations can be tuned by changing λ_D see **Fig. 3**. Surprisingly pearl necklaces exist in a second region at very strong screening, but distinguished by complete ionization. In that regime, the total electrostatic interaction within a pearl is not reduced because of partial charging but due to strong screening. Obviously this mechanism is not included in the DRO theory.

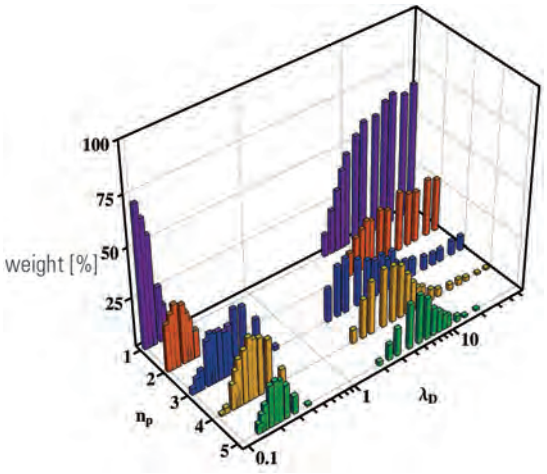

Fig. 3: Pearl necklace population at varying screening length λ_D, where n_p is the number of pearls.

By performing extensive grand canonical Monte Carlo simulations of annealed PELs in poor solvents, we have shown that variable screening can be used to establish a fine tuning of the structure of weak PELs. In **Fig. 4**, the results are combined in schematic phase diagrams in both the rather-poor-solvent regime and the close-to-Θ-point regime. In particular in the latter regime, we find a complex phase behavior of both highly and weakly charged structures.

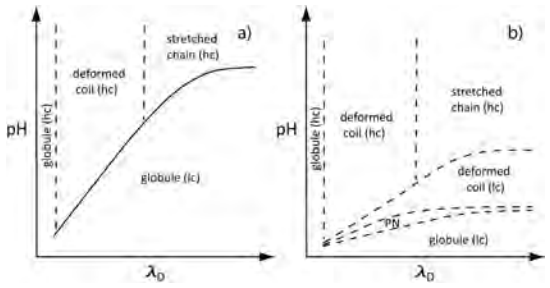

Fig. 4: Schematic phase diagram of weak PELs in poor solvent in a) the rather-poor-solvent regime and b) the close-to-Θ-point regime. The solid line in case a) indicates a first-order phase transition between high-charge states (hc) and low-charge state (lc). In case b), the hc-lc transition is a continuous one. Continuous transitions are represented by dashed lines. Note that hc globules occurring at strong screening can split into pearl necklaces (see Fig. 3) that are, however, quite different from usual DRO pearl necklaces denoted by PN.

C. Seidel, S. Uyaver[*)]
seidel@mpikg.mpg.de
[*)] present address: T. C. Maltepe University Istanbul

References:

[1] Raphael, E. and Joanny, J.-F.: Annealed and quenched polyelectrolytes. Europhys. Lett. **13**, 623-628 (1990).
[2] Netz, R. R.: Charge regulation of weak polyelectrolytes at low- and high-dielectric-constant substrates. J. Phys.: Condens. Matter **15**, S239-S244 (2003).
[3] Uyaver, S. and Seidel, C.: First-order conformational transition of annealed polyelectrolytes in a poor solvent. Europhys. Lett. **64**, 536-542 (2003).
[4] Uyaver, S. and Seidel, C.: Pearl-necklace structures in annealed polyelectrolytes. J. Phys. Chem. B **108**, 18804-18814 (2004).
[5] Kirwan, L. J., Papastavrou, G., Borkovec, M. and Behrens, S. H.: Imaging the coil-to-globule conformational transition of a weak polyelectrolyte by tuning the polyelectrolyte charge density. Nano Lett. **4**, 149-152 (2004).
[6] Uyaver, S. and Seidel, C.: Effect of varying salt concentration on the behavior of weak polyelectrolytes in a poor solvent. Macromolecules **42**, 1352-1361 (2009).
[7] Dobrynin, A. V., Rubinstein, M. and Obukhov, S. P.: Cascade of transitions of polyelectrolytes in poor solvents. Macromolecules **29**, 2974-2979 (1996).

Motor Cycles and Operation Modes of Kinesin

Steffen Liepelt 20.01.1979
2003: Diploma, Physics
(Humboldt-University, Berlin)
Thesis: A Stochastic Neuron Model as an Information Processing Unit.
2007: PhD, Physics
(MPI of Colloids and Interfaces, Potsdam)
Thesis: Energy Transduction in Network Models of Molecular Motors
Since 2007: Postdoc,
(MPI of Colloids and Interfaces, Potsdam)

Kinesin is a motor protein that moves directly along rigid cytoskeletal filaments (microtubules) to transport intracellular cargo. The energy for this transport is supplied by the hydrolysis of adenosine-triphosphate (ATP) to adenosine-diphosphate (ADP) and an inorganic phosphate group (P). For small load forces, each individual motor step of kinesin is coupled to the hydrolysis of exactly one ATP molecule and displaces the center of mass by 8 nm towards the microtubule plus-end. The different chemical reactions and conformational transformations of a motor molecule constitute its specific chemomechanical network. The cycles of this network govern the dynamics of the molecular motor.

Catalytic Action and Processive Walk

Kinesin consists of two identical amino acid chains dimerized in a coiled coil. One end of the protein dimer binds to cargo particles, while at the other end, each of the two chains forms a globular head-domain, which is able to bind to microtubules. The motor heads do not only mediate the binding of kinesin to the microtubule track, but also contain a catalytic site for ATP hydrolysis, see **Fig. 1**.

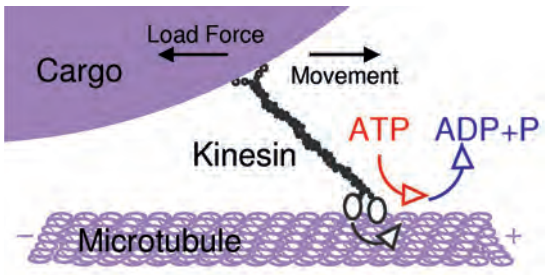

Fig. 1: The kinesin motor actively transports intracellular cargo towards the plus-end of microtubules. The motor stepping against a load force is driven by the hydrolysis of ATP to ADP and P.

The energy μ_T gained from binding an ATP molecule is partly released as $\mu_D+\mu_P$ by the unbinding of the hydrolysis products (ADP+P). The difference $\Delta\mu=\mu_T-(\mu_D+\mu_P)$ defines the chemical energy supply that can be used to perform mechanical work $W=L\,F$ via a translation of the motor by a step length L against a load force F, see **Fig. 2**.

Conservation of energy leads to the released heat $Q=\Delta\mu-W$. We have established the thermodynamics for the cycles of chemomechanical networks for molecular motors, **[1, 2]**. As a result, we obtained balance conditions for directed cycles that serve as constraints and ensure thermodynamic consistency. The obtained relations quantitatively connect thermodynamic control parameters of the motor environment with variables of the motor kinetics.

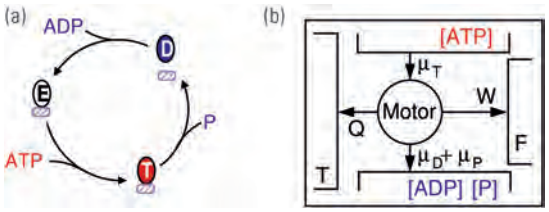

Fig. 2: (a) ATP hydrolysis cycle for an individual kinesin motor head. Each motor head may be occupied by ATP (T) or ADP (D), or be empty (E). In contrast to the E and T heads, the D heads are only weakly bound to the microtubule. (b) Energy flux diagram for a molecular motor, which is coupled to particle reservoirs with densities [ATP], [ADP], and [P], to an external load F and to a heat bath of temperature T.

Enzymatic Network Representations

The conformational state space for the dimeric kinesin molecule includes nine states as shown in **Fig. 3 (a)**. These states are connected by two types of transitions. Chemical transitions correspond to ligand binding or release events, as introduced in **Fig. 2 (a)**. Mechanical transitions correspond to the movement of the trailing motor head to the leading position, which translates the whole motor molecule by a step length L. In a systematic analysis we showed **[3, 4]**, that the main motor properties as observed in single molecule experiments by several groups as well as biochemical experiments concerning the processive walk of kinesin are described by a relatively simple model that is based on a seven state sub-network. This part of the general nine state network is composed of the three fundamental directed cycles $F1^+=|12561>$, $F2^+=|12571>$, and $B^+=|45234>$. As one can see from **Fig. 3 (b)**, the seven state network contains two additional cycles apart from the fundamental forward and backward stepping cycles, $F1^+$, $F2^+$, and B^+, namely $D1^+=|1234561>$ and $D2^+=|1234571>$. On these latter pathways the kinesin motor consumes ATP without stepping in any direction.

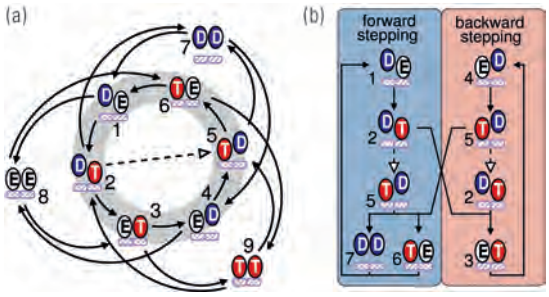

Fig. 3: (a) Network representation of the dimeric kinesin motor. While solid lines represent chemical transitions (with arrows indicating the ATP hydrolysis direction), the dashed line represents a mechanical transition (where a forward step corresponds to traveling of the weakly bound trailing head to the leading position). (b) The relevant seven state sub-network for the processive walk of kinesin.

Motor Velocity and ATP Hydrolysis Rate

The dynamics of the motor molecule is determined by excess fluxes $\Delta J(C^+)$ for each directed cycle C^+ of its chemomechanical network. In the seven state network, the motor velocity is given by $v=L(\Delta J(F1^+)+\Delta J(F2^+)-\Delta J(B^+))$, whereas the ATP hydrolysis rate is obtained from $h=\Delta J(F1^+)+\Delta J(F2^+)+\Delta J(B^+)+2(\Delta J(D1^+)+\Delta J(D2^+))$. The dicycle excess fluxes are functions of the rates that characterize each transition of the motor network. Because the transition rates by themselves depend on the three concentrations [ATP], [ADP], and [P] as well as on the load force F, the excess fluxes and consequently the motor velocity and the ATP hydrolysis rate become functions of these four thermodynamic control parameters. For fixed product concentrations [ADP] and [P], the motor velocity and hydrolysis rate can be expressed as functions of the load force and the chemical potential difference $\Delta\mu=\ln(K^{eq}[ATP]/([ADP][P]))$, where K^{eq} is the equilibrium constant for ATP hydrolysis, see **Fig. 4**. While the zeros of the motor velocity $v(F_s, \Delta\mu)=0$, for a given chemomechanical potential difference $\Delta\mu$, define the stall force F_s, the zeros of the ATP hydrolysis rate $h(F, \Delta\mu_b)=0$, for a given load force F, define the balancing chemical potential difference $\Delta\mu_b$.

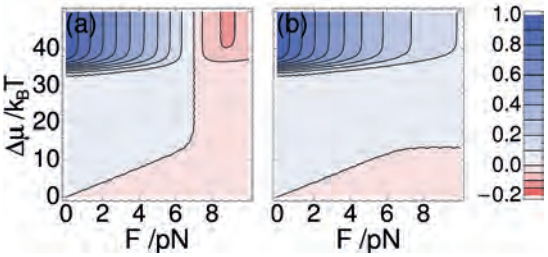

Fig. 4: (a) Motor velocity v and (b) ATP hydrolysis rate h as functions of load force F and chemical potential difference $\Delta\mu$ for fixed product concentrations [ADP]=[P]=0.5μM. Shown are the relative values with respect to $v(F=0, \Delta\mu\to\infty)$ and $h(F=0, \Delta\mu\to\infty)$.

Operation Mode Diagram for Kinesin

In **[5]** we derived explicit results for the stall force $F_s(\Delta\mu)$ and the balancing potential $\Delta\mu_b(F)$. It turned out that the dependence of the latter two quantities on the hydrolysis product concentrations [ADP] and [P] is rather weak for the relevant scales. While the stall force separates forward and backward stepping modes, the balancing potential separates ATP hydrolyzing and ATP synthesizing modes of the motor. In this way the (F, $\Delta\mu$) plane is divided up into four operation mode regions, see **Fig. 5**.

The operation mode diagram displayed in **Fig. 5** predicts for example, that the stall force F_s increases linearly with the chemical potential difference for $\Delta\mu<\Delta\mu_b(F\to\infty)=14\,k_BT$, but remains constant for larger $\Delta\mu$. Moreover, ATP synthesis against a positive chemical potential difference $\Delta\mu$ by pulling the kinesin motor into the backward direction can only be induced in the small $\Delta\mu$ regime. Thus, the operation mode diagram of the seven state network for kinesin provides explicit predictions that can be tested by future experimental studies.

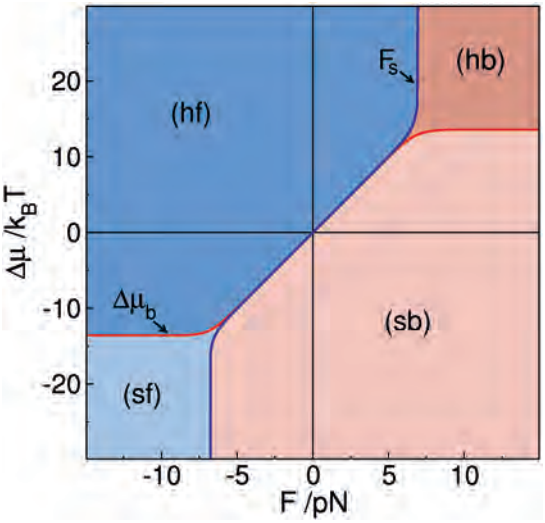

Fig. 5: Operation modes of the kinesin motor in the (F, $\Delta\mu$)-plane. The stall force F_s (blue line) separates forward and backward stepping modes. The balancing potential $\Delta\mu_b$ (red line) on the other hand, separates ATP hydrolyzing and synthesizing modes.

S. Liepelt, A. Valleriani, and R. Lipowsky,
liepelt@mpikg.mpg.de.

References:

[1] Liepelt, S., Lipowsky, R.: Steady-state balance conditions for molecular motor cycles and nonequilibrium stochastic processes. EPL **77**, 50002 (2007).

[2] Lipowsky, R., Liepelt, S.: Chemomechanical Coupling of Molecular Motors: Thermodynamics, Network Representations, and Balance Conditions. J. Stat. Phys. **130**, 39 (2008).

[3] Liepelt, S., Lipowsky, R.: Kinesin's Network of Chemomechanical Motor Cycles. Phys. Rev. Lett. **98**, 258102 (2007).

[4] Valleriani, A., Liepelt, S., Lipowsky, R.: Dwell time distributions for kinesin's mechanical steps. EPL **82**, 28011 (2008).

[5] Liepelt, S., Lipowsky, R.: Operation modes of the molecular motor kinesin. Phys. Rev. E **79**, 011917 (2009).

Cooperative Transport by Molecular Motors

Melanie J.I. Müller 23.10.1977
2004: Diploma, Physics
(University of Münster)
Thesis: Fluctuations of Critical Interfaces on Different Length Scales
2008: PhD, Physics
(Max Planck Institute of Colloids and Interfaces, Potsdam)
Thesis: Bidirectional Transport by Molecular Motors
Since 2008: Postdoc
(Max Planck Institute of Colloids and Interfaces Potsdam)

The complex internal structure of cells depends to a large extent on the targeted transport of vesicles, organelles and other types of cargo. This traffic is powered by molecular motor proteins that can be thought of as cellular 'nano-trucks' and transport cargo along cytoskeletal filaments, the cellular 'roads'. These filaments possess an intrinsic direction: they have a 'plus' and a 'minus' end. Some motors such as kinesin-1 walk to the plus end, while others such as cytoplasmic dynein walk to the minus end. Unlike trucks, however, the molecular motors constantly undergo thermal collisions with water molecules and therefore fall off their track after a certain distance. This run length is typically of the order of 1 µm.

Motors Team up to Pull a Cargo

In the cell, molecular motors work in teams, i.e. a single cargo is usually transported by more than one motor. For example, a cargo may be transported by several kinesin motors as depicted in **Fig. 1(a)**. Because of thermal collisions with water molecules, the motors unbind from and rebind to the filament in a stochastic manner. This means that the number of motors pulling the cargo fluctuates in time. We have studied the transport of a cargo pulled by several motors both theoretically and experimentally **[1, 2]**. In a biomimetic in vitro experiment, we monitored beads pulled by several kinesins. The number of kinesins on the beads was changed in a controlled manner by incubating the beads in solutions with varying kinesin concentration c, which is directly proportional to the average number of kinesin on the bead.

The main effect of a larger number of motors is an increase in the run length of the cargo, see **Fig. 1(b)-(h)**. The intuitive reason for this increase is that, when one motor unbinds from the track, the other bound motors still provide a connection between the cargo and the filament, and give the unbound motor a chance to rebind to this filament. We have successfully fitted our experimental results with our theoretical model, see the lines in **Fig. 1(b)-(h)**. This allowed us to determine the maximal number of motors pulling the beads to vary between two and seven motors for the concentrations shown in **Fig. 1**.

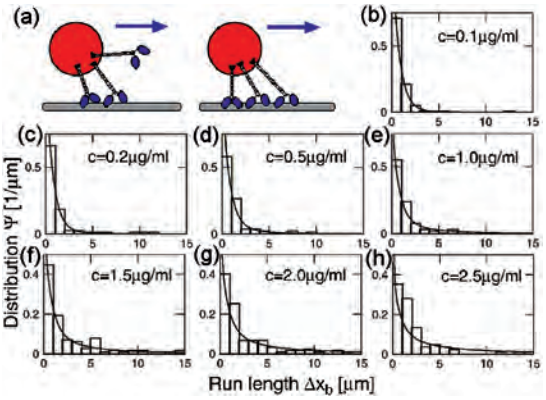

Fig. 1: Cargo transport by several kinesin motors. (a) A (red) cargo is pulled by three (blue) kinesins which unbind from and bind to the filament in a stochastic manner. (b)-(h) Experimental run length distributions (histograms) and theoretical fits (lines) for varying kinesin concentrations c. The probability of higher run lengths increases with concentration c.

Motors Play Tug-of-War

In the cell, many cargoes travel back and forth along cytoskeletal filaments, changing direction every few seconds. Since one type of motor can walk only into one direction, two types of motors must be present on such bidirectional cargoes. Indeed, cellular cargoes are often transported by several plus-end moving kinesins and several minus-end moving dyneins. This leads to the problem of coordinating motors that walk into opposite directions, see **Fig. 2(a)**. Naively, one would expect that the motors should block each other, leading to almost no cargo motion as depicted in **Fig. 2(d)**. However, cellular cargoes are observed to move rapidly back and forth as shown in **Fig. 2(e)**. This transport pattern implies that during plus motion, only plus motors are active **(Fig. 2(b))** and during minus motion, only minus motors are active **(Fig. 2(c))**. How is this cooperation accomplished?

In order to explain the observed bi-directional transport, several groups have postulated a coordination machinery that organizes the motors into states (b) and (c) and prevents state (a) in **Fig. 2**. However, we have recently developed a model which can explain the experimental observations without such an extra machinery **[3, 4]**. In our model, the motors manage to organize themselves by playing tug-of-war: The plus motors pull on the minus motors and vice versa. This force leads to an increased tendency of the motors to drop off the filament.

If, for example, more plus than minus motors are bound to the filament, the force on each minus motor is higher than the force on each plus motor. This higher force increases the probability for a minus motor to unbind from the filament. As soon as one minus motor has unbound, the remaining bound minus motors have to sustain the plus motor's force alone. This increases the unbinding probability of the minus motors even further and leads to a cascade of minus motor unbinding events until no minus motor is left – the cargo ends up in a state with only plus motors bound, as shown in **Fig. 2(b)**, and quickly moves into the plus direction. This plus motion persists until the stochastic unbinding and binding events of the motors lead to a cargo state for which more minus than plus motors are bound to the filament. Then an unbinding cascade of the plus motors leads to a state with only minus motors bound, see **Fig. 2(c)** and therefore to fast minus motion. In total, the cargo stochastically switches between fast plus and minus motion, see **Fig. 2(e)**. Our tug-of-war model can thus explain the experimentally observed bi-directional motion without postulating an unknown coordination machinery.

We have compared the results of our model to experiments on the transport of lipid droplets in fly embryos performed by Steven Gross and co-workers from the University of California in Irvine, USA. Our model was able to explain their experimental observations quantitatively.

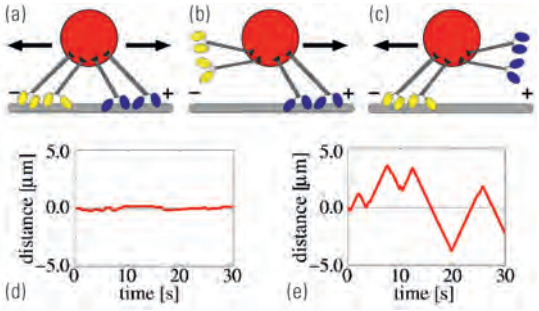

Fig. 2: Tug-of-war of molecular motors. (a)-(c) A (red) cargo particle is transported by two (blue) kinesins moving to the plus end (right) and two (yellow) dyneins moving to the minus end (left). In (a), the opposing motors block each other, so that the cargo has essentially zero velocity, as shown by the trajectory in (d). In (b) and (c), by contrast, only one type of motors is bound and can move the cargo quickly to the plus or minus end, respectively. A cargo alternating between states (b) and (c) moves quickly back and forth as shown in (e).

Motor Traffic with Internal States

If many molecular motors walk along the same filament, the traffic may become congested. We have studied this situation theoretically, taking into account that stepping of a molecular motor is a complex process which consists of a series of transitions between different motor states **[5]**. We have considered the simplest case of two internal states.

We have found that even for only two internal states, some properties of the motor traffic exhibit a strong and surprising dependence on the detailed kinetics of the step. For example, the effective unbinding rate of the motors may both increase and decrease with increasing motor density, see **Fig. 3(a)**. Likewise, the run length either exhibits a strong decrease or almost no dependence on the motor density, see **Fig. 3(b)**. These results may help to clarify controversial experimental results on motor unbinding rates and run lengths for high motor densities.

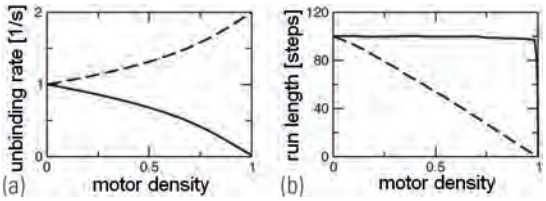

Fig. 3: Molecular motor traffic with internal states: (a) Unbinding rate and (b) run length as a function of motor density, which can vary between 0 and 1. Depending on the details of the stepping kinetics, the motors may exhibit increasing unbinding and decreasing run length (dotted lines), or decreasing unbinding and largely constant run lengths (solid lines).

M. J.I. Müller, J. Beeg, F. Berger, Y. Chai, R.S. Gracià, R. Dimova, R. Lipowsky
melanie.mueller@mpikg.mpg.de

References:

[1] Klumpp, S. , Müller, M.J.I., and Lipowsky, R.: Traffic of molecular motors, in: Traffic and Granular Flow '05, edited by A. Schadschneider, T. Pöschel, R. Kühne, M. Schreckenberg, and D. E. Wolf, Springer, Berlin, pp. 251-261 (2007).

[2] Beeg, J., Klumpp, S., Dimova, R. , Gracià, R. S., Unger, E. and Lipowsky, R.: Transport of beads by several kinesin motors, Biophys. J. **94**, 532-541 (2008).

[3] Müller, M.J.I., Klumpp, S., and Lipowsky, R.: Tug-of-war as a cooperative mechanism for bidirectional cargo transport by molecular motors, Proc. Natl. Acad. Sci. USA **105**, 4609-4614 (2008).

[4] Müller, M.J.I. , Klumpp, S., and Lipowsky, R.: Motility states of molecular motors engaged in a stochastic tug-of-war, J. Stat. Phys. **133**, 1059-1081 (2008).

[5] Klumpp, S., Chai, Y., and Lipowsky, R.: Effects of the chemomechanical stepping cycle on the traffic of molecular motors, Phys. Rev. E **78**, 041909 (2008).

Morphologies of Vesicles Loaded with Aqueous Polymer Solution

Rumiana Dimova 06.04.1971
1995: Diploma, Chemistry (Sofia University, Bulgaria), Major: Chemical Physics and Theoretical Chemistry, Thesis: Role of the Ionic-Correlation and the Hydration Surface Forces in the Stability of Thin Liquid Films
1997: Second MSc (Sofia University, Bulgaria) Thesis: Interactions between Model Membranes and Micron-Sized Particles
1999: PhD, Physical Chemistry (Bordeaux University, France) Thesis: Hydrodynamical Properties of Model Membranes Studied by Means of Optical Trapping Manipulation of Micron-Sized Particles
2000: Postdoc (Max Planck Institute of Colloids and Interfaces, Potsdam)
Since 2001: Group Leader (Max Planck Institute of Colloids and Interfaces, Potsdam)

When a water drop is placed on a surface, it can attain the shape of a spherical cap, or it can flatten and spread. The interaction between the surface and the drop can be characterized by the contact angle. Zero or nonzero contact angle correspond to complete or partial wetting, respectively. Varying parameters such as temperature or liquid composition, one can cause the system to undergo a transition from complete to partial wetting. Examples for such transitions are not abundant. Some have been found for fluid-fluid interfaces in binary mixtures and for liquids at solid substrates. Liquid droplets at chemically patterned or topographically structured surfaces can also undergo morphological wetting transition, which reflects the freedom of the contact angles at pinned contact lines.

Recently, we discovered a complete to partial wetting transition occurring for an aqueous solution enclosed within a freely suspended lipid vesicle **[1]**. Here the substrate is a lipid membrane, permeable to water and with the thickness of a few nanometers.

Lipid vesicles have long been recognized as models for the cell membrane and have been widely used to study the properties of lipid membranes **[2]**. Recently, it has been found that giant unilamellar vesicles loaded with aqueous solutions of water-soluble polymers may exhibit several spatial compartments formed by phase separation within the vesicle interior. Thus, these artificial cell-like systems are a biomimetic setup for studying molecular crowding, fractionation and protein sorting in cells.

To study wetting transitions in vesicles, we encapsulated a homogeneous aqueous solution composed of poly(ethylene glycol) (PEG) and dextran in giant vesicles made of dioleoylphosphatidylcholine (96 mol %), and G_{M1} ganglioside (4 mol %). In order to obtain vesicles containing two phases, the vesicles were deflated osmotically by adding a hypertonic solution to the external medium in a stepwise manner.

Partial-to-Complete Wetting Transition

The polymer solution loaded in the vesicles is in the one-phase state at room temperature **(Fig. 1A)**. As the osmolarity of the external medium is increased, water is forced out of the vesicle in order to balance the resulting osmotic pressure. As a result, the polymer concentration inside the vesicle is raised and phase separation occurs **(Fig. 1B)**. Since the dextran-rich phase is heavier than the PEG-rich phase, the newly formed spherical dextran-rich droplet is always located at the bottom of the vesicle **(Fig. 1C)**. As the osmolarity of the external medium is further increased, the dextran-rich phase starts to wet the membrane **(Fig. 1D)**. The contact area between the dextran-rich phase and the membrane grows with increasing osmolarity; see **Fig. 1D-F**. The morphology change of the dextran-rich droplet indicates a wetting transition from complete wetting of the PEG-rich phase or complete dewetting of the dextran-rich phase in **Fig. 1B, C** to partial wetting in **Fig. 1D-F**.

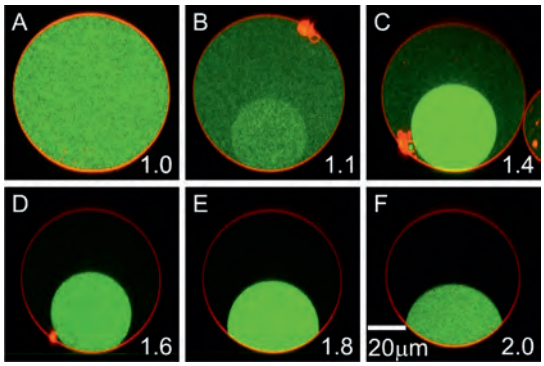

Fig.1: Confocal micrographs of a vesicle (vertical cross sections), encapsulating polymer solution with of 4.05 wt % PEG, Mw = 8 kg/mol, and 2.22 wt % dextran, Mw = 400 - 500 kg/mol. 0.52 wt % of the total dextran is labeled with fluorescein isothiocyanate (green). The membrane is labeled with 0.1 mol % dipalmytoylphosphatidylcholine-rhodamine (red). Initially, the polymer solution inside the vesicle is in the one-phase state (A). The vesicle is subjected to hypotonic solution and deflates inducing phase separation (B, C). Upon further deflation, the dextran-rich drop (green) undergoes wetting transition (D-F). The numbers on the snapshots indicate the osmolarity ratio between the external medium and the initial internal polymer solution. The system was left to equilibrate for at least 2 hours after each consecutive osmolarity change.

The overall vesicle shape seems to remain spherical during the deflation steps. The volume of the vesicle decreases with increasing osmolarity. The excess membrane area gained in this way forms a cluster of interconnected small vesicles and lipid aggregates partially visible in **Fig. 1B, C, D**.

Fitting the vesicle and the drop contours in the acquired images with spherical caps, allows us to obtain the vesicle volume under different osmolarity conditions. Because the membrane is not permeable to the polymers, the number of polymer molecules inside the vesicle is fixed and the decrease of vesicle volume is due to the loss of water. Thus, we can calculate the total polymer concentration in the vesicle at different osmolarities. In addition, the vesicle geometry allows us to measure the contact angle Θ, between the dextran-rich phase and the membrane (see inset in **Fig. 2**). The cosine of the contact angle Θ, defines the wettability via $\cos(\Theta) \equiv (\Sigma_{pm} - \Sigma_{dm}) / \Sigma_{pd}$, where Σ_{pm}, Σ_{dm} and Σ_{pd} are the interfacial tensions at the interfaces between the PEG-rich phase and the membrane (pm), the dextran-rich phase and the membrane (dm), and the PEG-rich phase and the dextran-rich phase (pd). The wettability as a function of the total polymer concentration inside the vesicle is given in **Fig. 2**. A sharp change in the contact angle is observed for polymer concentration 8.5 wt %, indicating a wetting transition.

After this transition point, the wettability of the dextran-rich phase increases with the polymer concentration as shown in **Fig. 2**.

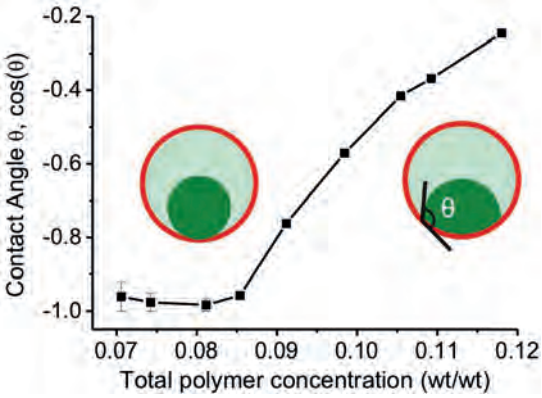

Fig. 2: The cosine of the contact angle Θ (see the right inset for definition) versus the total polymer concentration in the vesicle. The weight ratio between dextran and PEG is 0.55. The insets schematically illustrate the dewetted and wetted states.

We consider a possible mechanism involved in the observed wetting transition. When the polymer solution is close to the mixing point, the composition difference between the phases is very small, which leads to extremely low interfacial tension Σ_{pd}. When the latter is smaller than $|\Sigma_{pm}-\Sigma_{dm}|$, the membrane is fully wetted by the PEG-rich phase. Both Σ_{pd} and $|\Sigma_{pm}-\Sigma_{dm}|$ increase with increasing polymer concentration, but Σ_{pd} increases faster than $|\Sigma_{pm}-\Sigma_{dm}|$ because the compositions of both phases change, but the composition of the membrane does not. When $\Sigma_{pd}=|\Sigma_{pm}-\Sigma_{dm}|$, the wetting transition occurs, and the dextran-rich phase starts to wet the membrane. Vesicle simulations based on dissipative particle dynamics may offer a possible way to reveal the order of this wetting transition. Work in this direction is in progress.

Wetting-Induced Budding

When both phases wet the membrane, the smaller one may bud out of the vesicle body upon further deflation. **Fig. 3** shows such an example. The vesicle with two liquid phases is approximately spherical at low osmolarity ratio between the external medium and the initial internal polymer solution; see **Fig. 3B**. When the vesicle is further dehydrated, the dextran-rich phase starts to form a bud away from the PEG-rich phase; see **Fig. 3C**. The excess area arising from dehydration is utilized by the vesicle to undergo morphological changes. In this way, the area of the liquid two-phase interface is decreased significantly. As the osmolarity of the medium is increased further, the dextran-rich phase may form a complete bud leading to a dumbbell-like vesicle where the area of the two-phase interface is almost zero.

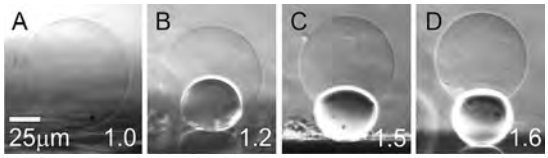

Fig. 3: Side-view phase contrast images of a vesicle sitting on a glass substrate. After phase separation (A, B), further deflation causes the dextran-rich phase to bud out (C, D). The dense part at the lower part of the vesicle is the dextran-rich phase. The light part is the PEG-rich phase. Note that the dextran was not fluorescently labeled in this vesicle as in Fig. 1. The numbers on the snapshots indicate the osmolarity ratio between the external medium and the initial internal polymer solution. The system was left to equilibrate for at least 2 hours after each consecutive osmolarity change.

The presence of the interfacial tension Σ_{pd} causes a pulling force on the membrane towards the vesicle interior. When Σ_{pd} is small, the membrane tension can easily balance this pulling in the normal direction. The excess area arising from dehydration can be stored in the form of lipid aggregates or tethers **[3, 4]**, and the vesicle can remain spherical. As Σ_{pd} increases and the vesicle deflates further (creating more excess area), the membrane tension can no longer sustain the spherical vesicle shape. Because the membrane is very flexible it bends along the interface of the liquid phases and budding of the dextran-rich phase occurs as the vesicle is further deflated. The budding event significantly reduces the interfacial energy by decreasing the contact area between the liquid phases.

R. Dimova, Y.H. Li, R. S. Gracià, A. Grafmüller
rumiana.dimova@mpikg.mpg.de

References:

[1] Li, Y., Lipowsky, R. and Dimova, R.: Transition from complete to partial wetting within membrane compartments. J. Am. Chem. Soc. **130**, 12252-12253 (2008).
[2] Dimova, R., Aranda, S., Bezlyepkina, N., Nikolov, V., Riske, K. A., Lipowsky, R.: A practical guide to giant vesicles. Probing the membrane nanoregime via optical microscopy. J. Phys.: Condens. Matter **18**, S1151-S1176 (2006).
[3] Li, Y., Gracià, R. S., Lipowsky, R. and Dimova, R.: in preparation.
[4] Li, Y. PhD Thesis: Phase separation in giant vesicles (2009).

Morphological Transitions of Vesicles in AC Electric Fields

Rumiana Dimova 06.04.1971
1995: Diploma, Chemistry (Sofia University, Bulgaria), Major: Chemical Physics and Theoretical Chemistry, Thesis: Role of the Ionic-Correlation and the Hydration Surface Forces in the Stability of Thin Liquid Films
1997: Second MSc (Sofia University, Bulgaria) Thesis: Interactions between Model Membranes and Micron-Sized Particles
1999: PhD, Physical Chemistry (Bordeaux University, France) Thesis: Hydrodynamical Properties of Model Membranes Studied by Means of Optical Trapping Manipulation of Micron-Sized Particles
2000: Postdoc (Max Planck Institute of Colloids and Interfaces, Potsdam)
Since 2001: Group Leader (Max Planck Institute of Colloids and Interfaces, Potsdam)

Electromagnetic fields are widely generated by power transmission lines, home appliances and electronics for telecommunication. Thus, our bodies are always exposed to them. This raises the question: "How do biological cells react to electromagnetic fields?" Giant vesicles provide an excellent model system for the cell because their typical size (~10 μm) is of the same linear order and their fundamental structure presents a closed compartment encapsulated by a lipid bilayer membrane. The cell-size dimensions of giant vesicles allow us to observe them directly by optical microscopy. Furthermore, it is possible to systematically change the salinities of the internal and external solutions of the vesicles. Studies of giant vesicles exposed to alternating (AC) electric fields are a good start to clarify the interactions between biological cells and electromagnetic fields from the viewpoint of physics and chemistry **[1]**.

In AC electric fields, spherical vesicles can assume different shapes: spheres, prolate ellipsoids, and oblate ellipsoids. Recently, we reported the morphologies of the vesicles for a wide range of field frequencies **[1, 2]**. We found that the conductivities of the solutions had an important influence on the shapes of the vesicles and mapped those on a morphological diagram as a function of the field frequency and conductivity condition. The latter was characterized by the ratio of the conductivities of the internal vs. the external solutions: $x=\lambda_{in}/\lambda_{ex}$. On the basis of the experimental findings, we have theoretically clarified the mechanisms of the four types of morphological transitions discovered in the experiments **[3-5]**.

Experimentally Determined Morphological Transitions

Giant vesicles made of the conventional egg lecithin were prepared with different conductivity of the internal and external solutions, i.e. various conductivity ratios x. The vesicles were spheres in the absence of AC fields. They were subjected to AC fields systematically varying the field frequency ω. The vesicle deformation was visualized with phase contrast microscopy.

Fig. 1 shows the obtained morphological diagram of the vesicle shapes in AC fields. The vesicles are spheres at high frequency independent of the conductivity ratio x. When $x>1$, the spherical vesicles are deformed into prolates with decreasing frequency. The frequency of this transition is about 1-10 MHz, see transition 1 in **Fig. 1**. The vesicles remain prolate when decreasing the frequency further for $x>1$. On the other hand, when $x<1$, the spherical vesicles at high frequency change their shapes to oblates with decreasing frequency. The characteristic frequency of this transition is about 10 MHz (transition 2). The vesicles remain oblate in the frequency range from about 10 kHz to about 10 MHz. Note that for $x>1$, the vesicles are prolate in the same frequency range. Thus, there is a morphological transition at $x \cong 1$ from oblate to prolate in the course of increasing x while keeping the frequency constant (transition 3). When further decreasing the frequency, the oblate vesicles for $x<1$ change to prolates at the transition frequency of about 1 kHz (transition 4).

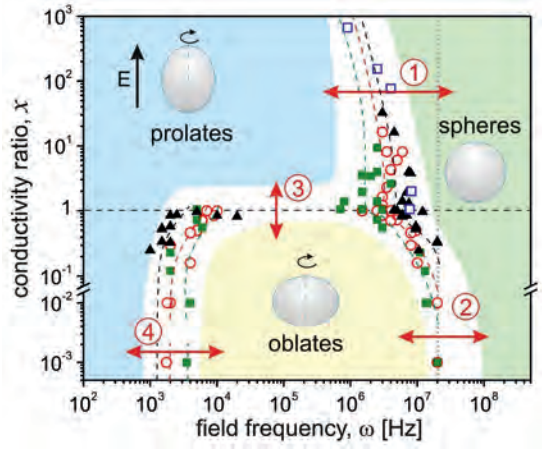

Fig. 1: Morphological diagram of giant vesicles in AC electric fields for a wide range of conductivity conditions and field frequencies. The conductivities of the internal solutions are fixed to 1.5 mS/m (filled squares), 6.5 mS/m (open circles), 13 mS/m (filled triangles), and 1000 mS/m (open squares). The broken lines are just a guide to the eye and the shaded areas indicate zones of specific morphology. The limit of the experimentally accessible frequency (2×10^7 Hz) is indicated by the dotted vertical line.

Theoretically Predicted Shape Deformations

The conductivities and the field frequency determine the conduction currents and displacement currents through the system, respectively. We have studied the mechanisms of the morphological transitions from the point of view of the current flow through the system. The developed approach extends a previous model (Winterhalter and Helfrich, J. Coll. Interf. Sci. 122, 1987) to include the effect of asymmetric conductivity conditions and the frequency dependence of the conductivity **[3-5]**. Analytical expressions of the transition frequency were derived **[4]**. The theoretically calculated morphological diagram, plotted in **Fig. 2**, agrees well with the experimental observations as shown in **Fig. 1**.

In the low frequency regime, the shapes of the vesicles are prolate independent of x. Lipid membranes are insulators, and both conduction currents and displacement currents flowing across the membranes are negligible in the low frequency regime ($\omega < 1$ kHz). As a result, the electric fields are tangential to the surface of the vesicles and do not penetrate into the vesicle interior but avoid the high impedance membrane. Maxwell stresses arise from the tangential electric fields and squeeze the vesicles at the equator: the vesicles are deformed into prolates.

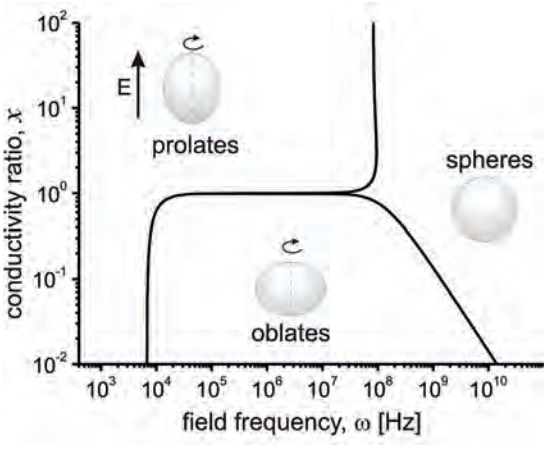

Fig. 2: The morphological diagram of vesicles in AC electric fields predicted theoretically. The calculation was carried out for vesicles with radius 20 µm. The membrane was assumed to have thickness of 4 nm and bending stiffness of 2×10^{-19} J. The conductivity of the internal solutions is 6.5 mS/m [4].

With increasing frequency, the displacement currents across the membrane grow together with the component of the electric field normal to the vesicle surface. In the intermediate frequency regime, this normal component generates shear Maxwell stresses. The latter compete with the Maxwell stresses, which deform the vesicles into prolates in the low frequency regime. The shear Maxwell stresses arising from the normal electric fields are the origin of the prolate-oblate transition 4 in **Fig. 1**.

In the intermediate frequency regime, electric charges accumulate at the interfaces of the vesicles because of the normal electric fields. The electric charge density and the corresponding net charges across the membrane depend on the conductivity condition. Within the continuum theory, these charges arise from the discontinuity of the permittivities across the interfaces and represent local accumulation of cations and anions at these interfaces. **Fig. 3** gives schematic snapshots of the electric charge distributions. They experience forces by the tangent electric fields denoted as f in **Fig. 3**. This force acts parallel to the tangent electric fields to deform the vesicles into prolates when $x>1$, and perpendicular to the tangent electric fields to deform the vesicles into oblates when $x<1$. The flip of polarity of the electric charges at $x \sim 1$ provides the mechanism of transition 3 in **Fig. 1**.

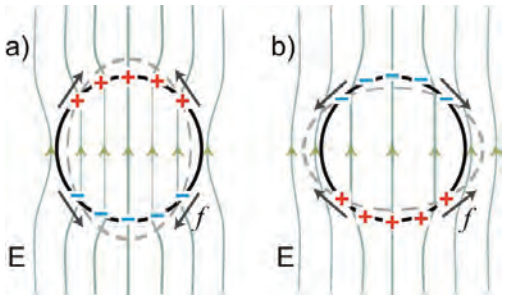

Fig. 3: At intermediate frequencies, electric charges accumulate at the vesicle interfaces. Due to the difference in the conductivity conditions, the net charges across the membrane (illustrated with pluses and minuses) differ depending on the value of x. The force applied to the charges by the tangential electric fields (f) deforms the vesicles (a) into prolates for x>1 and (b) oblates for x<1, which leads to transition 2 in Fig. 1.

In the high frequency regime, the shapes of the vesicles are spherical independent of x. The time required to charge the vesicles is characterized by the Maxwell-Wagner charging time. For higher frequency, the net electric charges across the membrane interface decay with the field frequency, and at frequencies larger than the inverse Maxwell-Wagner charging time, the electric charges cannot follow the oscillation of the electric fields. This changes the shapes of the vesicles from prolate ($x>1$) or oblate ($x<1$) to spherical, see transition 1 and 2 in **Fig. 1**.

In summary, the distributions of the electric fields by the displacement currents and the electric charges accumulated by the Maxwell-Wagner mechanisms play important roles in the morphological transitions of vesicles in AC electric fields.

R. Dimova, S. Aranda, T. Yamamoto, P. Vlahovska
rumiana.dimova@mpikg.mpg.de

References:

[1] Dimova, R., Riske, K., Aranda, S., Bezlyepkina, N., Knorr, R. and Lipowsky, R.: Giant vesicles in electric fields. Soft Matter **3**, 817-927 (2007).

[2] Aranda, S., Riske, K. A., Lipowsky, R. and Dimova, R.: Morphological transitions of vesicles induced by alternating electric fields. Biophys. J., **95**, L19-L21 (2008).

[3] Aranda, S. PhD Thesis: Deformation of model membranes subjected to electric fields (2009).

[4] Yamamoto, T., Aranda, S., Dimova, R. and Lipowsky, R.: in preparation.

[5] Vlahovska, P. M., Graciá, R. S., Aranda, S. and Dimova, R.: Electrohydrodynamic model of vesicle deformation in alternating electric fields; in press Biophys. J.

Lipid Flow Patterns in Vesicles

Rumiana Dimova 06.04.1971
1995: Diploma, Chemistry (Sofia University, Bulgaria), Major: Chemical Physics and Theoretical Chemistry, Thesis: Role of the Ionic-Correlation and the Hydration Surface Forces in the Stability of Thin Liquid Films
1997: Second MSc (Sofia University, Bulgaria)
Thesis: Interactions between Model Membranes and Micron-Sized Particles
1999: PhD, Physical Chemistry (Bordeaux University, France)
Thesis: Hydrodynamical Properties of Model Membranes Studied by Means of Optical Trapping Manipulation of Micron-Sized Particles
2000: Postdoc (Max Planck Institute of Colloids and Interfaces, Potsdam)
Since 2001: Group Leader (Max Planck Institute of Colloids and Interfaces, Potsdam)

When applied to colloidal systems, electric fields induce various phenomena, which have found wide application in micro- and nano-technologies in the past decade. Neutral particles (droplets, bubbles, lipid vesicles, solid beads) suspended in a medium of different polarizability acquire charge at their surfaces when exposed to electric fields. The interaction of the field with the surface charges results in a surface force that may cause particle deformation, kinetic effects, electro-osmotic fluid flows, etc.

In the case of uniform electric fields applied to lipid vesicles, the radial component of the electric surface force leads to a shape deformation at weak field strengths (see section "Morphological transitions of vesicles in AC electric fields" on page 122) or causes membrane rupture, at strong fields **[1]**. The lateral component, on the other hand, may induce fluid flows, analogous to the flows induced in liquid droplets. However, there is a fundamental difference between droplets and vesicles, which arises from the properties of the lipid bilayer. The membrane behaves as a two dimensional nearly incompressible fluid. It develops tension to keep its surface area constant.

Under homogeneous alternating (AC) fields, membrane flow in the vesicle is not expected because the lateral electric stress is counterbalanced by the resulting axially symmetric gradient in the membrane tension. In inhomogeneous fields however, this force balance is broken and a flow of lipids occurs in order to restore it. Note that in most experimental chambers and conditions used for electro-manipulation, vesicles, cells or other particles experience inhomogeneous fields, due to screening by neighbors, sedimentation, chamber geometry, or other factors.

To study the membrane dynamics in AC fields, we used giant vesicles made of lipid mixtures, which at room temperature phase separate into liquid ordered (Lo) and liquid disordered (Ld) phases. The membrane was composed of saturated and unsaturated lipids and cholesterol; for more information on the vesicle preparation see **[2]**. A tiny fraction of fluorescent dye was added, which preferentially partitions in the Ld phase. The lipid ratio was such that the Lo phase appeared as dark circular patches in the surrounding fluorescently labeled Ld phase.

The membrane flow pattern was resolved by following the motion of the Lo patches with confocal microscopy. The bottom and the top part of the vesicle were recorded as shown on the micrographs in **Fig. 1 a-c**. The inner and outer vesicle solutions were 0.1 M sucrose and glucose, respectively. This ensures an osmotic balance, i.e. constant vesicle volume, and causes the vesicles to sediment at the bottom of the chamber since sucrose solutions have higher density than glucose solutions with the same concentration. The electric field was applied between two parallel cylindrical electrodes. The proximity of the bottom glass to the vesicle leads to an asymmetric field distribution at its surface. The field strength is much higher at the lower vesicle part, facing the glass, than at the top part, see **Fig. 2**.

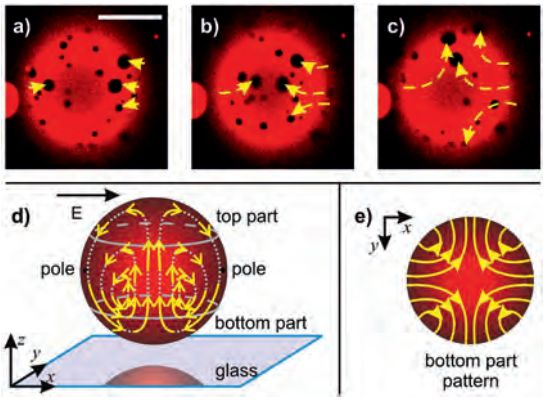

Fig. 1: Confocal micrographs illustrating the membrane flow on the bottom part (a-c) of a giant vesicle about 150 µm in diameter induced by an AC field (360 V/cm, 80 KHz), at an external conductivity of 25 mS/m. The vesicle was prepared from a mixture of 4.8 : 3.2 : 2 dioleoylphosphatidylcholine : dipalmitoylphosphatidylcholine : cholesterol. The time between the consecutive snapshots is approximately 1.3 s. The yellow dashed arrows indicate the trajectories of selected domains in the consecutive snapshots. The scale bar corresponds to 50 µm. The vesicle is located close to the bottom of the observation chamber as illustrated in (d), where the vesicle top and bottom parts, the poles and the field direction are indicated. The side and the bottom views of the flow lines are sketched in (d) and (e), respectively. The length of the arrows in (d) indicates the flow velocity.

Such asymmetric field distribution leads to a special membrane flow pattern consisting of concentric closed trajectories, organized in four symmetric quadrants, each extending from the bottom to the top of the vesicle as in **Fig. 1d, e**. The flow is fastest at the periphery of the quadrant and at the bottom of the vesicle. The top and the bottom of the vesicle are stagnation points. The velocity of the domains reaches about 30 µm/sec corresponding to laminar flows. It can be further enhanced by the field strength and the conductivity of the external solution. Interesting effects are observed when the field frequency is varied. At frequencies less than about 3 MHz, the motion in the circular trajectories is directed downwards past the poles and upwards along the equator as sketched on **Fig. 1d** but at higher frequencies it reverses its direction.

The calculation of the lateral electric stress or surface force density on the membrane suggests that the vesicle experiences larger stress in the vicinity of the solid substrate **[2]**. As a result, a non-uniform and non-symmetric membrane tension builds up. It triggers lipid flow towards the regions of highest tension, similarly to Marangoni flows in monolayers. Interestingly, the frequency at which we observe reversal of the flow direction, i.e. around 3 MHz, coincides with the Maxwell-Wagner frequency, above which the polarization of the vesicle is determined by the media permittivities. Thus, the reversal of the flow direction may arise from the difference between the permittivities of the glucose and the sucrose solutions.

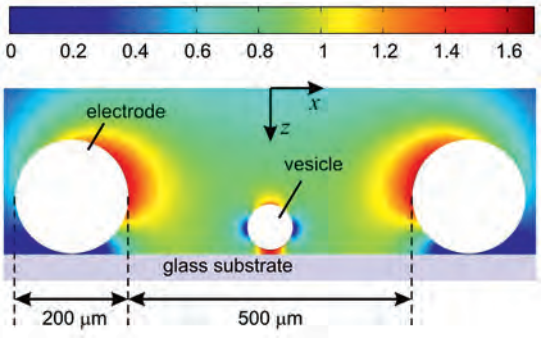

Fig. 2: Electric field distribution at 100 kHz in a cross section of the chamber consisting of two parallel cylindrical electrodes fixed to a glass substrate. The image displays a cross section passing through the centre of a vesicle located in the middle between the electrodes. The vesicle is 40 µm in radius and is located at 8 µm above the glass. The media conductivity is 0.3 mS/m. The field inside the vesicle is not shown. The data are rescaled with the strength of a field, which would be induced between two parallel planar electrodes at a distance of 500 µm.

To investigate the lipid flow driven by the electric field, we theoretically model the dielectric polarization of the vesicle by placing image electric dipoles and quadrupoles at the center of the vesicle. The calculated Maxwell stresses arising from asymmetric electric fields are found to induce flow patterns, which agree with the experimental observations **[3]**.

The flow in the membrane is coupled to fluid flows in the internal and external media. To visualize the effect of the membrane flow on the internal medium we used vesicles containing aqueous solution of the water-soluble polymers poly-(ethylene glycol) (PEG) and dextran (see section "Morphologies of Vesicles loaded with Aqueous Polymer Solutions" on page 120). At specific polymer concentration, this solution can undergo phase separation **[4]** producing droplets of dextran-rich phase, which can be visualized e.g. by fluorescently labeled dextran. The droplets tend to coarsen slowly. Before the coarsening is completed we subject such vesicles to asymmetric AC fields. As expected, the droplets start to move because of the coupling to the membrane flow. Therefore, when a cross section of the vesicle is observed with confocal microscopy as in **Fig. 3**, the droplets are observed to come into focus and to go out of focus again.

These AC field-induced flows in giant vesicles have possible applications in microfluidic technologies. Giant vesicles in inhomogeneous AC fields or in hydrodynamic flows mimicking, e.g., the situation of red blood cells in capillaries may be used as nano-reactors for fluid manipulation, i.e. displacing, mixing, trapping, etc. To demonstrate lipid mixing, we performed experiments where lipid vesicles composed of only one Lo and one Ld domains, are exposed to an AC field for a certain period of time. One example is shown in **Fig. 4**. The field-induced membrane flow causes domain fission leading to the appearance of a large number of smaller domains. For sufficiently strong membrane flows, the number of domains grows with the time of exposure. The growing number of domains, on the other hand, increases the probability of domain encounter and fusion. Domain fusion counterbalances the fission and therefore, the domains will reach a stationary state characterized by a certain size distribution after a certain time.

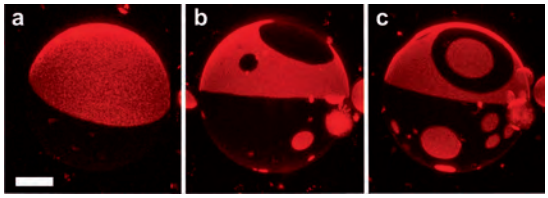

Fig. 4: 3D confocal scans of the lower vesicle hemisphere illustrating lipid mixing induced by AC field (80 kHz, 500 V/cm), at an external conductivity of 0.25 mS/m. The vesicle with a diameter about 95 µm was prepared from a mixture of 2.66 : 5.33 : 2 dioleoylphosphatidylcholine : dipalmitoylphosphatidylcholine : cholesterol. (a) Before applying the field, the vesicle has only two domains, which break apart after continuous field exposure of (b) 2 min and (c) 3 min. The scale bar corresponds to 25 µm.

We were not able to achieve similar mixing of dextran-rich and PEG-rich phases starting from a state, where the two phase are fully separated, because the pressure of the internal flow was not large enough to overcome the surface tension between the two polymer phases. However, in other systems, e.g. vesicles enclosing suspensions of micro-particles, the induced flows may be used to homogenize the internal vesicle content.

R. Dimova, M. Staykova, T. Yamamoto, Y. Li
rumiana.dimova@mpikg.mpg.de

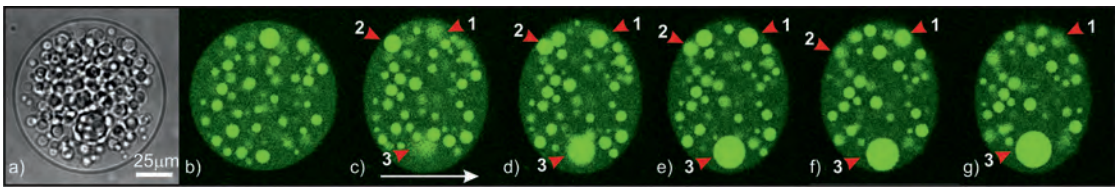

Fig. 3: (a) A phase-contrast images and (b-g) confocal cross sections of a giant lipid vesicle enclosing dextran-rich droplets (green fluorescence) in a PEG-rich phase. The cross section in (b), corresponding to the image in (a), is taken close to the equatorial plane of the vesicle and shows only the droplets in focus. Application of an inhomogeneous AC field (460 V/cm, 80 KHz) at an external conductivity of 40 mS/m leads to a vesicle shape deformation and an internal flow, in the direction perpendicular to the plane of the image in (c-d). The flow is visualized by following the motion of droplets 1, 2 and 3, which come in focus and go out of focus. The time period is 2.5 s between images c)-d) and d)-e), and 5 s between e)-f) and f)-g). The field direction is indicated by the arrow in (c).

References:

[1] Dimova, R., Riske, K., Aranda, S., Bezlyepkina, N., Knorr, R. and Lipowsky, R.: Giant vesicles in electric fields. Soft Matter **3**, 817-927 (2007).

[2] Staykova, M., Lipowsky, R. and Dimova, R.: Membrane flow patterns in multicomponent giant vesicles induced by alternating electric fields. Soft Matter **4**, 2168-2171 (2008).

[3] Yamamtoto, T., Staykova, M., Dimova, R., Lipowsky, R.: in preparation.

[4] Li, Y., Lipowsky, R. and Dimova, R.: Transition from complete to partial wetting within membrane compartments. J. Am. Chem. Soc. **130**, 12252-12253 (2008).

Membranes and Nonpolar Surfaces

Volker Knecht 06.01.1970
1996: Diploma in physics (University of Kaiserslautern)
Thesis: Computer based renormalization group study of the two-dimensional XY model
1997: Software trainee (TECMATH GmbH, Kaiserslautern)
1998-1999: Software engineer (LMS Durability Technologies GmbH, Kaiserslautern)
2003: PhD, Physics (MPI of biophysical chemistry, Göttingen)
Thesis: Mechanical coupling via the membrane fusion SNARE protein syntaxin 1A: a molecular dynamics study
2003-2005: Postdoc (University of Groningen, the Netherlands)
2005-2006: Postdoc (MPI of Colloids and Interfaces, Potsdam)
Since 2006: Group Leader (MPI of Colloids and Interfaces, Potsdam)

Membranes

The function of biomembranes is not restricted to surrounding a cell and its various compartments as passive separation layers. By facilitating transport of molecules from one side to the other, they play also an active role. Membranes are composed of a complex mixture of various lipids and proteins, with the lipids forming a bilayer. Our aim is to understand biomembranes in terms of the self-organization of these constituents. The information about the molecular architecture of membranes accessible experimentally is very limited. Therefore, we use molecular dynamics simulation techniques to computationally model the cooperative processes underlying the mesoscopic properties of membranes. Molecular dynamics simulations based on numerically solving Newton's equations of motion to propagate a system in time and semi-empirical force fields to describe interatomic interactions may provide highly detailed information about the molecular properties of membranes. As a first step, we model membranes as lipid bilayers, see **Figs. 1-4 [1-3]**.

Membrane fusion is a key step for important processes including viral infection and drug delivery. For the first time, we have studied the fusion of lipid vesicles in atomic detail, see **Fig. 1 [1]**. This process involves the formation of a lipidic connection between two opposed bilayers denoted as stalk, (see **Fig. 1a**) and subsequent formation (see **Fig. 1b**) and rupture (see **Fig. 1c**) of a hemifusion diaphragm. This work opens the perspective to investigate a wide range of mesoscopic biological processes at atomic resolution.

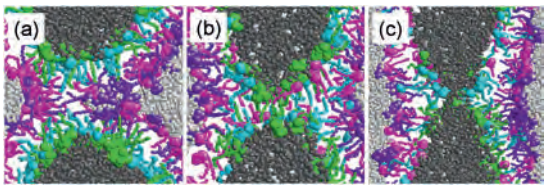

Fig. 1: Fusion of vesicles composed of dipalmitoyl-phosphateidylcholine (DPPC) and (protonated) palmitic acid (PA) in a molecular dynamics simulation in atomic detail [1]. (a) A stalk as well as a hemifusion diaphragm (b) before and (c) after rupture are depicted. Water and head group atoms are shown as spheres, tails are shown as bonds. Water is depicted in dark or light gray. Colors distinguish between DPPC (purple and green) and PA molecules and the leaflets where the molecules resided initially.

The free energy of early membrane fusion intermediates has been determined using simulations in conjunction with a coarse grained model, see **Fig. 2 [2]**. We find that the free energy of a stalk is lower than that of a pre-stalk intermediate which involves a single hydrated lipid tail. A peptide known to induce fusion in vitro does not change the free energy of stalks but does lower the free energy of the solvated tail intermediate. These results challenge assumptions of continuum models and support the idea that early fusion kinetics is determined by interbilayer flips of lipid tails.

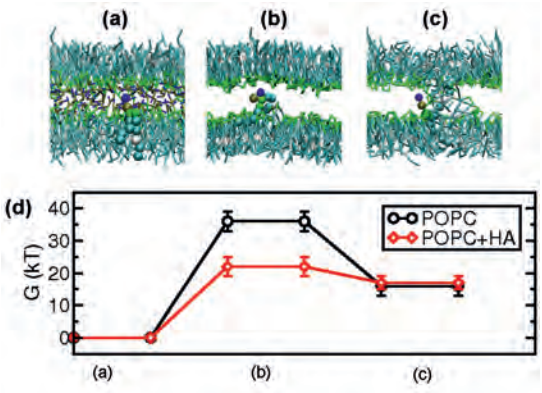

Fig. 2: Free energy of early membrane intermediates from molecular dynamics simulations in conjunction with a coarse grained model [2]. The system simulated was a palmitoyl-oleoyl-phosphateidylcholine (POPC) bilayer at low hydration fused with its periodic image (a-c). The bilayer at equilibrium (a), the transition state for interbilayer flips of a lipid tail (b), and a stalk (c) are depicted. (d) The free energies in the absence (black) and presence (red) of an influenza hemagglutinin fusion peptide are compared. In (a-c), lipids are shown as sticks and a selected lipid to which a harmonic potential was applied to induce the intermediates on the limited timescale of the simulations is highlighted. In (b,c), the choline and phosphate groups of the other lipids are omitted for clarity.

Peptides can also induce pores which is the putative mode of action of α-helical antimicrobial peptides. We are currently investigating the interaction of the antimicrobial peptide NK-2 with lipid bilayers. Membrane pores, though, can also form in the absence of peptides. In a recent study we have revealed that membrane nanopores, see **Fig. 3a**, correspond to a local free energy minimum, explaining previous data on transmembrane conductance and the metastability of nanopores observed in previous numerical studies **[3]**. In the same set of simulations, the free energy of lipid desorption, see **Fig. 3b**, has been calculated. Our results indicate that the free energies of lipid desorption from a bilayer or from a micelle differ, and that the critical micelle concentration is an inadequate reference for the energetics of lipid desorption from a bilayer unlike commonly assumed.

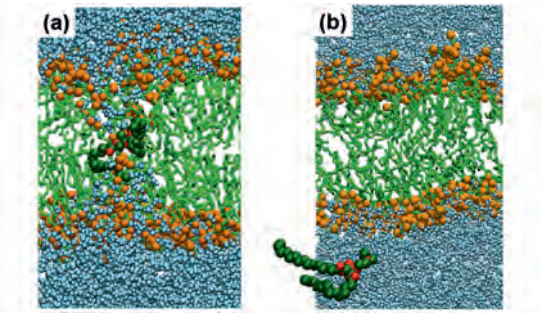

Fig. 3: The energetics of (a) nanopores and (b) lipid desorption for a DPPC bilayer were determined from atomistic simulations in which a harmonic potential was applied to a selected lipid [3]. Lipid tails are shown as green sticks and headgroups as orange spheres. The lipid subjected to the harmonic potential is highlighted. Water is shown in blue.

Understanding membranes at physiological conditions requires to investigate their interaction with ions. We are studying the interaction of potassium (K), sodium (Na), and lithium (Li) with zwitterionic phospholipid bilayers, see **Fig. 4(a,b)**. Potassium and sodium are the most abundant cations inside or outside a cell, respectively, whereas lithium intake can be curative or toxic depending on the dosage. We find that all of these cations are adsorbed at the headgroups of a zwitterionic lipid bilayer. The affinity increases in the order K<Na<Li and, thus, increases with decreasing size of the bare ion. These observations agree with results from electrophoresis experiments. In order to facilitate quantitative predictions on the affinity, an improved force field for alkali chlorides in water has been developed **[4]**. For the first time, we have used simulations to study cholesteryl hemisuccinate (CHEMS), an acidic cholesterol ester. CHEMS forms bilayers and is used as a subcomponent of liposomes for drug delivery. For CHEMS in the anionic state, the negative charge of the lipids is found to be almost fully compensated by (sodium) counterions adsorbed at the lipid headgroups, see **Fig. 4c**.

Lipid bilayers may also adsorb cationic peptides as observed for antimicrobial peptides. The antimicrobial peptide NK-2 is not only adsorbed at anionic but also at zwitterionic (phosphateidylethanolamine, PE) lipids while it does not interact with (zwitterionic) phosphateidylcholine (PC) lipids, as indicated from electrophoretic mobilities. We address the question how NK-2 distinguishes between prokaryotic and eukaryotic membranes. The hypothesis that, at physiological conditions, the underlying mechanism is not simply charge complementarity as commonly assumed but more specific molecular interactions, is currently tested.

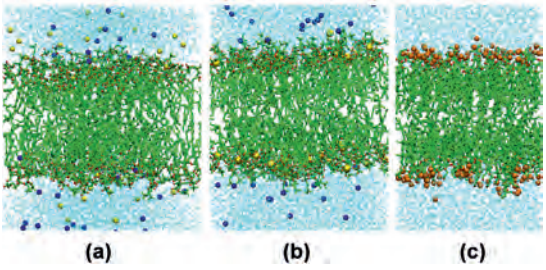

Fig. 4: Adsorption of ions to lipid bilayers. A POPC bilayer in an aqueous LiCl solution (a) before and (b) after a 100 ns simulation as well as (c) an anionic CHEMS bilayer with Na counterions after a 100 ns simulation are depicted. Lipids are shown as green sticks. Lipid oxygen atoms (red) are indicated. Ions are shown as spheres whose colors distinguish between Li (yellow), Cl (blue), and Na (orange).

Electrophoresis of Neutral Particles

Though widely used to assess the surface charge of colloidal particles, electrophoresis experiments may be misleading, as indicated by simulations in our group. For more than a century, electrophoretic mobilities of hydrophobic particles in water have been interpreted in terms of negative surface charges from the adsorption of hydroxide (OH^-). In contrast, recent spectroscopic and simulation studies have indicated significant surface affinity for hydronium (H_3O^+) but not for hydroxide. In simulations we observe that neutral wax slabs in water in the presence of an electric field but in the absence of ions migrate as though they were negatively charged, see **Fig. 5 [5]**. This work may resolve the controversy between the electrophoretic and spectroscopic studies and supports the view that neat water at hydrophobic surfaces is acidic.

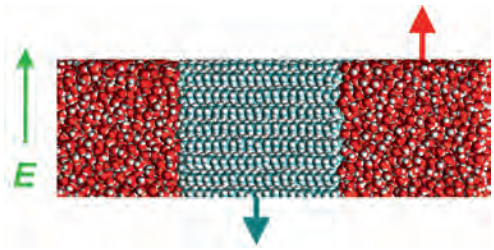

Fig. 5: Electrophoresis of neutral particles in simulations. A wax slab (hexatriacontane, C36) parallel to an external electric field in water in the absence of ions migrates as if it was negatively charged. Colors distinguish between carbons (cyan), oxygen (red), and hydrogen (white). The direction of the electric field (green) and the motion of wax (cyan) and water (red) are indicated.

V. Knecht, N. Awasthi, Y. Chai, C. v. Deuster, M. Kittner, B. Klasczyk, A. Krukau, Y. Smirnowa
vknecht@mpikg.mpg.de

References:

[1] Knecht, V., Marrink, S.J.: Molecular dynamics simulations of lipid vesicle fusion in atomic detail, Biophys. J. **92**, 4254-4261 (2007).

[2] Smirnowa, Y., Marrink, S.J., Lipowsky, R., Knecht, V.: Pre-stalk transition state for membrane fusion includes hydrated lipid tail, in preparation.

[3] Grafmüller, A., Lipowsky, R., Knecht, V.: Energetics of membrane nanopores and lipid desorption, submitted.

[4] Klasczyk, B., Lipowsky, R., Knecht, V.: Kirkwood-Buff force field for alkali chlorides in water, in preparation.

[5] Knecht, V.: Water at hydrophobic surface is acidic: re-interpretation of electrophoretic mobilities.

Tension Induced Membrane Fusion

Andrea Grafmüller 18.08.1980
2004: Master (MSci) , Physics (Queen Mary, University of London, London, UK)
Thesis: Computer Simulation of Kinetic Ising Systems with Glauber Dynamics
2007: PhD, Theoretical Physics (Max Planck Institute for Colloids and Interfaces, Potsdam)
Thesis: The Fusion of Membranes and Vesicles
2007-2009: Postdoc (Max Planck Institute for Colloids and Interfaces, Potsdam)

Fusion of biological membranes is an essential process in many areas of cell biology, ranging from vesicular trafficking and synaptic transmission to cell-cell fusion and viral fusion. Lipid vesicles, which are often used as simplified model systems for the rather complex biological membranes, can also be induced to fuse experimentally by a variety of methods.

Since it is currently not possible to resolve the length and time scales of membrane fusion experimentally, we use a mesoscopic simulation technique, dissipative particle dynamics (DPD), to probe the molecular details and energy barriers of the fusion process **[1-4]**. We focus on the presumably simplest way to induce fusion between a vesicle and a planar bilayer, namely via membrane tension.

The stochastic nature of the process makes it necessary to simulate a large number of fusion attempts in order to obtain reliable fusion statistics and to extract meaningful values for the fusion probability and the average fusion times.

A Molecular Picture of the Fusion Pathway

All successful fusion events follow the same pathway shown in **Fig. 1**. In this fusion pathway, configurations of individual lipids play an important role.

Upon first contact, the vesicle adheres to the planar membrane patch, forming a relatively sharp contact angle. Fusion starts with individual lipids at this 'kink' assuming a splayed tail configuration with one tail inserted in each membrane. This disturbs the local double-bilayer structure and leads to the formation of a disordered membrane domain within the contact zone where the hydrophobic regions of the two bilayers are in direct contact, and which expands following the contact line in a bean-like shape. Finally, within this disordered region, lipids reorder to form a small hemifused patch, which expands for a short time and finally ruptures at the rim to form the fusion pore.

Overall, the fusion process can be decomposed into three sub-processes. (i) Sub-process α corresponds to the first lipid tails moving into the other bilayer, (ii) sub-process β consists of the nucleation of the hemifused patch and (iii) sub-process γ corresponds to the rupture of this patch and formation of the fusion pore.

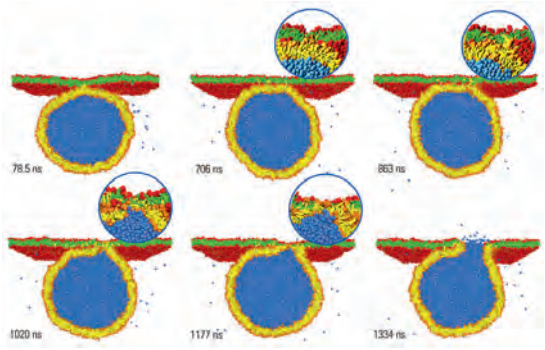

Fig. 1: Fusion of a vesicle to a planar membrane. The vesicle consists of 6869 lipids (orange heads, yellow chains), the planar membrane contains 6911 lipids (red heads, green chains). The water beads originally inside the vesicle are blue, those outside are not shown for clarity. The six snapshots illustrate the development of the fusion event from 78.5 ns after the first contact until the fusion pore opens after 1334 ns. The insets are magnifications of the lipid rearrangements at the contact line.

Fusion Probability and Alternative Pathways

When two tense membranes come into contact they may fuse. Alternatively, tense membranes may rupture or, at lower tensions, either the hemifused patch might expand without rupturing, thereby gaining membrane area and relaxing the membrane tension or the adhering state might remain stable.

Because of these other possibilities, the fusion probability depends strongly on the membrane tension as can be seen in **Fig. 2**. The probability of successful fusion is high for an optimal intermediate tension, but decreases steeply for smaller tensions as adhesion and hemifusion become more favourable. As the tension decreases, the fusion probability seems to vanish before the tensionless membrane state is attained. This would imply that the tension has to exceed a certain threshold value in order to induce fusion **[3, 4]**.

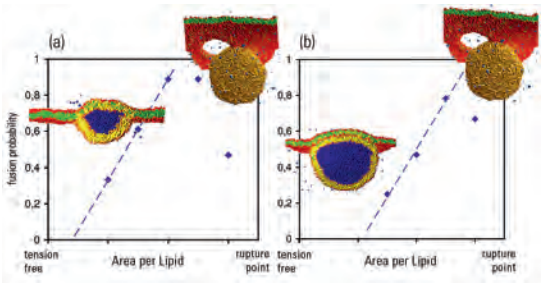

Fig. 2: Fusion probability as a function of molecular area for vesicles with a diameter of (a) 14 nm and (b) 28 nm. In both cases, the fusion probability depends strongly on the tension with a maximum at an optimal value. At higher tensions, fusion becomes less likely because of membrane rupture; at lower tensions, fusion is more and more replaced by hemifusion or adhesion.

Fusion Time Distribution and Energy Barriers

The tension determines not only the success rates, but also the time scale of fusion. At lower tensions (i) the fusion times become larger and (ii) the fusion time distributions become broader. From the statistics of the fusion time together with separate simulations in which one lipid was pulled into a splayed conformation, the energy barriers for the fusion observed in these simulations could be estimated **[2, 3]**.

Fig. 3 shows the average fusion time as a function of the molecular area. It appears to grow exponentially with decreasing tension. This exponential growth of the fusion times together with the decreasing fusion probability makes it exceedingly difficult to determine the time scale of fusion from computer simulations as the tensionless state is approached.

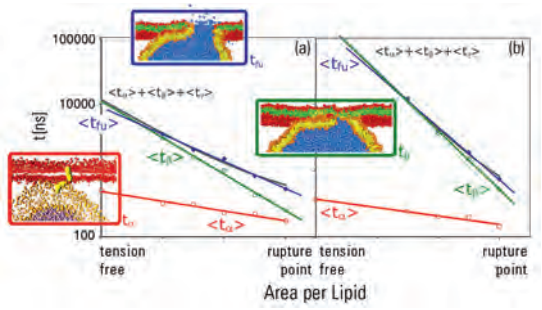

Fig. 3: The average duration of the tension dependent sub-processes α (red circles) and β (green diamonds) displayed together with the average fusion time (blue diamonds) as a function of the area per molecule for vesicles with a diameter of (a) 14 nm and (b) 28 nm. Both times depend exponentially on the area per molecule. The three insets show the final states of the sub-processes.

The average duration of the sub-processes α and β, both decrease exponentially with increasing tension, as shown in **Fig. 3**. This implies that the corresponding energy barriers should depend linearly on the membrane tension. The timescale of sub-process γ on the other hand, is found to vary between 150 ns and 300 ns, independent of both tension and vesicle size.

Since the sub-process α involves the movement of single lipids, relative to their surroundings, it is accessible to direct simulation. In two adhering membranes, a single lipid tail was pulled slowly with a harmonic potential from its original position into the other bilayer, so that the lipid assumes a splayed conformation as observed in the fusion simulations. The average work required for this process in 20 independent simulations was found to be $9 \pm 2\,k_BT$. This value constitutes an upper bound for the energy barrier and should correspond to the barrier itself for very slow pulling. Using the Jarzynski relation on this data leads to a similar barrier height of $8\,k_BT$.

The energy barrier for this process is provided by the (partially) hydrated polar head groups of the proximal monolayers. In the coarse-grained simulations it is implemented via one specific interaction parameter. Simulation enforcing a splayed lipid conformation, have shown, that the height of the barrier is primarily governed by the value of this parameter. Thus the barrier size can be tuned in such a way that it is consistent with available reference data such as the hydration energy of one hydrocarbon chain.

Using the information obtained in these simulations in the fits to the other timescales, the energy barriers corresponding to the other sub-processes for a tension free membrane can be estimated to be $10-15\,k_BT$ and $8\,k_BT$. At low tensions the total fusion time is dominated by the timescale of hemifusion. Thus the simulation statistics suggest that the main energy barrier for fusion of tensionless membranes is of the order of $10-15\,k_BT$ **[2,3]**.

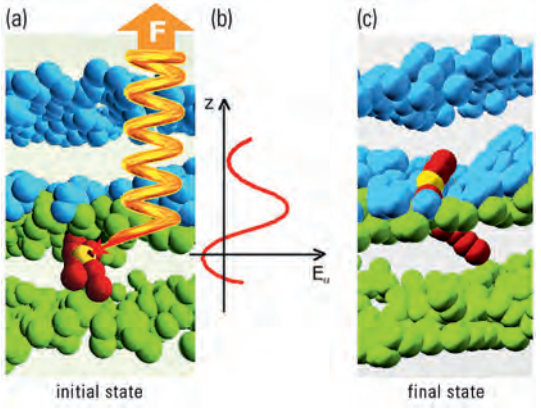

Fig. 4 Simulations of enforced lipid flips used to measure the corresponding energy barrier (a) From two adhering bilayers (head beads blue/green, tail beads omitted for clarity) a single lipid is selected (orange heads, yellow/red tails) and a force F arising from a slowly moving harmonic potential is applied to one of its tail beads (red), until the tail has flipped to the other bilayer, so that the lipid has assumed a splayed configuration with one tail inserted in each bilayer as shown in (c). (b) Energy landscape for the bead as a function of the displacement z of the yellow bead. It has a high barrier in the centre corresponding to the repulsive head groups and increases to the sides reflecting displacement of the head group into the hydrophobic region.

A. Grafmüller, J. Shillcock, R. Lipowsky
andrea.grafmueller@mpikg.mpg.de

References:

[1] J. Shillcock and Reinhard Lipowsky: Tension-induced fusion of bilayer membranes and vesicles. Nature materials **4**, 225-228 (2005).

[2] A. Grafmueller, J. Shillcock and R. Lipowsky: Pathway of membrane fusion with two tension dependent energy barriers. Phys. Rev. Lett. **98**, 218101 (2007).

[3] A. Grafmüller, J. Shillcock and R. Lipowsky: The Fusion of Membranes and Vesicles-Pathway and Energy Barriers from Dissipative Particle Dynamics. Biophys. J. **96**, 1-18 (2009)

[4] A. Grafmueller, J. Shillcock and R. Lipowsky: Dissipative Particle Dynamics of Tension induced Membrane Fusion, Molecular Simulation, (accepted Nov. 2008)

Membrane Adhesion

Thomas Weikl 01.04.1970
1996: Diploma, Physics
(Freie Universität Berlin)
Thesis: Interactions of rigid membrane inclusions
1999: PhD, Physics
(Max Planck Institute of Colloids and Interfaces, Potsdam)
Thesis: Adhesion of multicomponent membranes
2000-2002: Postdoc
(University of California, San Francisco)
Since 2002: Group Leader
(Max Planck Institute of Colloids and Interfaces, Potsdam)
2008: Habilitation, Physics
(University Potsdam)
Thesis: Transition states and loop-closure principles in protein folding

Biological membranes are the "skin" of cells. On the one hand, membranes separate the cell interior from the environment. On the other hand, they allow a vital exchange of matter. In addition, they are involved in central biological processes such as photosynthesis and recognition. The membranes are elastic and can attain a multitude of different shapes. The elastic properties depend on the different lipids and proteins that constitute the membranes.

Membrane Domains at Corrugated Substrates

Biological membranes contain a multitude of lipid molecules. Although the lipid molecules diffuse quickly through the fluid membranes, they are not homogeneously distributed. Instead, they tend to form domains that are either rich or poor in cholesterol. The cholesterol-rich domains are stiffer than the cholesterol-poor domains, which has direct implications on the membrane curvatures. The membrane curvatures, in turn, influence the domain formation. Curvature and domain formation thus depend on each other.

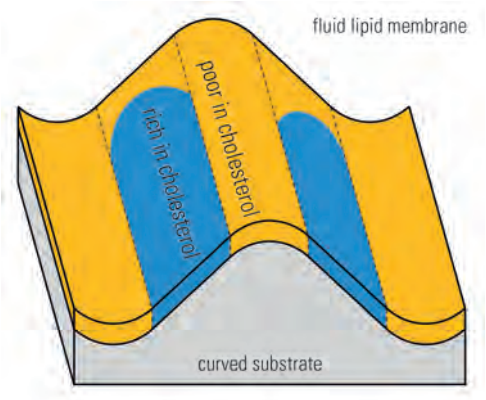

Fig. 1: Fluid lipid membrane on a corrugated, solid substrate. The membrane contains domains that are rich (blue) or poor (yellow) in cholesterol. The cholesterol-rich domains are stiffer than the cholesterol-poor domains and tend to avoid the curved parts of the membrane along the ridges and valleys of the substrate, provided the line tension between the domains does not exceed a certain threshold value.

The question now is: Can curvatures that are imposed on the membrane, e.g. by a corrugated substrate, cause stable domain patterns? In general, it is difficult to control the size of lipid domains since they readily coalesce and grow into larger and larger structures. However, if the membranes adhere to a substrate with a geometrically structured surface, the stiffer cholesterol-rich domains tend to avoid the curved parts of the membrane. The resulting domain patterns are stable as long as the curvature of the substrate surface exceeds a threshold value that depends on the line tension of the domains boundaries **[1]**. Below this threshold, a single cholesterol-rich domain forms, which covers many ridges and valleys of the substrate.

These theoretical arguments explain patterns that have already been observed in experiments. They might also help to understand why biological membranes exhibit only small domains rich in cholesterol, while in artificial, "biomimetic" membranes rather large domains are formed. In contrast to artificial membranes, biological membranes are attached to the cytoskeleton of the cell, i.e. to a network of polymers that actively curves the membranes. Besides other active cell processes, these curvatures could stabilize membrane patterns with small cholesterol-rich domains.

Interactions Mediated by Adhesive Particles

The adjustment of surface interactions is crucial for controlling the adhesiveness of biological cells and membranes. These interactions are often dominated by the composition of the membranes, but can also be affected by molecules or particles in the surrounding medium. The concentration of these particles is an additional control parameter for the membrane interactions, a parameter that is often easier to adjust than the membrane composition, and can be varied over a wider range than external parameters such as temperature.

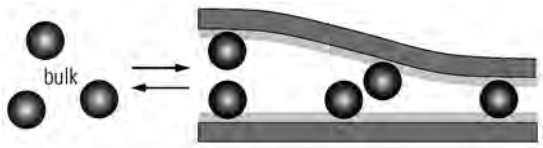

Fig. 2: Two membranes in contact with a solution of adhesive particles. A particle can bind the two membranes together if their separation is slightly larger than the particle diameter (particle on the right). At large separations, the particles can only bind to one of the membranes (particles on the left).

On the one hand, non-adhesive particles can induce attractive 'depletion' interactions between membranes or surfaces, because close contact of the surfaces reduces the excluded volume for the particles. On the other hand, adhesive particles can directly bind two membranes together if the membrane separation is equal to or slightly larger than the particle diameter, see **Fig. 2**. At larger separations, the particles can only bind to one of the membranes.

We find that the effective, particle-mediated adhesion energy of the membranes is given by

$$U_{ef} \approx \frac{k_B T}{d^2} \ln \frac{1 + q\phi e^{2U/k_B T}}{\left(1 + q\phi e^{U/k_B T}\right)^2} \qquad (1)$$

for small volume fractions Φ and large binding energies U of the adhesive particles **[2]**. Here, d is the particle diameter, T denotes the temperature, and q is a dimensionless parameter that depends on the range of the interaction between the particles and the membranes.

Interestingly, the effective adhesion energy (1) exhibits a maximum at an optimum volume fraction of the particles, see **Fig. 3**. At this volume fraction, the particle coverage of two planar parallel membranes turns out to be close to 50 % for large separations ('half coverage'), and 100 % ('full coverage') for short, binding separations. Bringing the membranes from large separations within binding separations thus does not 'require' desorption or adsorption of particles at the optimum volume fraction.

The effective adhesion energy (1) can be understood as a difference of two Langmuir adsorption free energies **[2]**. The adhesion energy can also be generalized to cases in which the adhesive particles or molecules specifically bind to receptors anchored in the membranes **[2]**. Examples are biotinylated lipids, which can be crosslinked by the protein streptavidin.

Diffusion of Receptor-Ligand Bonds

The adhesion of cells is mediated by membrane receptors that bind to complementary ligands in apposing cell membranes. It is generally assumed that the lateral diffusion of mobile receptor-ligand bonds in membrane-membrane adhesion zones is slower than the diffusion of unbound receptors and ligands. We have found that this slowing down is not only caused by the larger size of the bound receptor-ligand complexes, but also by thermal fluctuations of the membrane shape **[3]**. In our model, the fluctuations reduce the bond diffusion constant in planar membranes by a factor close to 2 in the biologically relevant regime of small bond concentrations. Active cell processes may enhance these membrane shape fluctuations **[4]**.

References:

[1] Rozycki, B., Weikl, T. R. and Lipowsky, R.: Stable patterns of membrane domains at corrugated substrates. Phys. Rev. Lett. **100**, 098103 (2008).

[2] Rozycki, B., Lipowsky, R. and Weikl, T. R.: Effective surface interactions mediated by adhesive particles. Europhys. Lett. **84**, 26004 (2008).

[3] Krobath, H., Schütz, G. J., Lipowsky, R. and Weikl, T. R.: Lateral diffusion of receptor-ligand bonds in membrane adhesion zones: Effect of thermal membrane roughness. Europhys. Lett. **78**, 38003 (2007).

[4] Rozycki, B., Weikl, T. R. and Lipowsky, R.: Stochastic resonance for adhesion of membranes with active stickers. Eur. Phys. J. E **22**, 97-106 (2007).

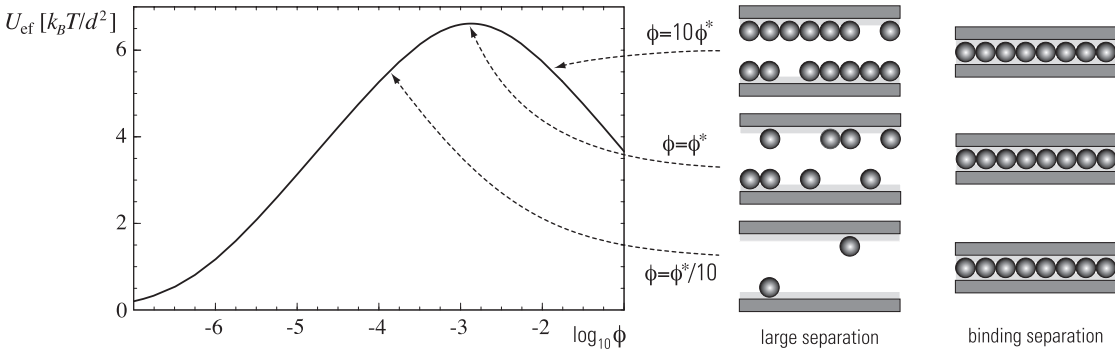

Fig. 3: Effective adhesion energy U_{ef} of the membranes, given in eq. (1), as a function of the particle volume fraction Φ for the binding energy $U = 8\,k_BT$ and $q = 0.25$. The effective adhesion energy is maximal at the optimal volume fraction $\Phi^* \approx \exp(-U/T)/q \approx 1.34\ 10^{-3}$. At the optimal volume fraction, the particle coverage of two planar parallel membranes is about 50 % for large separations, and almost 100 % for small separations at which the particles can bind to both membranes.

T. Weikl, J. Hu, H. Krobath, B. Rozycki
thomas.weikl@mpikg.mpg.de

Life Cycle of Chlamy Cells

Angelo Valleriani 14.03.1966
1992: Diploma, Physics (University of Bologna)
Thesis: Conformal Invariance, Renormalization Group and Integrable Models in Two-Dimensional Quantum Field Theories
1996: PhD, High-Energy Physics (SISSA-ISAS, Trieste)
Thesis: Form Factors and Correlation Functions
1996-1998: Postdoc, (Max Planck Institute for the Physics of Complex Systems, Dresden)
1998-2000: Postdoc (Max Planck Institute of Colloids and Interfaces, Potsdam)
Since 2000: Group Leader and IMPRS Coordinator, (Max Planck Institute of Colloids and Interfaces, Potsdam)

Chlamydomonas reinhardtii with the short name chlamy is a unicellular photosynthetic alga, see **Fig. 1a**, which is studied within the ongoing project GoFORSYS on systems biology. Large populations of cells are cultivated in a fermenter at the MPI of Molecular Plant Physiology, varying several environmental conditions such as light spectrum, light intensity, temperature, and nutrient concentrations. Samples of about one million cells are extracted from the fermenter to perform measurements that should shed light onto several aspects of the intracellular activity. As a result of these measurements, the metabolite concentrations are obtained as averages over a very large number of cells.

In general, the cells that contribute to these average properties differ in their age, size, and molecular composition. It is, thus, not obvious how these average quantities are related to the properties of single cells. In order to address this question, our project considers theoretical models for cell populations. As shown schematically in **Fig. 1b**, each cell undergoes a cell cycle that starts with the growth phase (G1), passes a commitment point for cell division, and then enters the other phases necessary for this division.

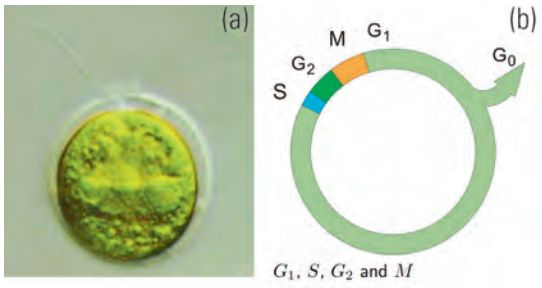

Fig. 1: (a) Image of one single cell of Chlamydomonas reinhardtii. (b) Schematic representation of the cell cycle of a single cell. The phase denoted by G1 is the growth phase; the other three phases prepare the cell for division. The phase G0 is a dormant or rest phase.

It turns out, that chlamy cells remain in the growth phase for a random amount of time and thus attain a relatively broad distribution of cell sizes. This implies that each mother cell can produce a number of daughter cells roughly proportional to its size and, thus, can undergo multiple divisions.

One global property of each cell is its volume which should determine the overall rate of energy consumption. Our first objective was therefore to develop a model for the cell size distribution under time-independent conditions that may be implemented in the fermenter. The model can be used to calculate stationary distributions, two examples are shown in **Fig. 2** corresponding to binary and multiple divisions.

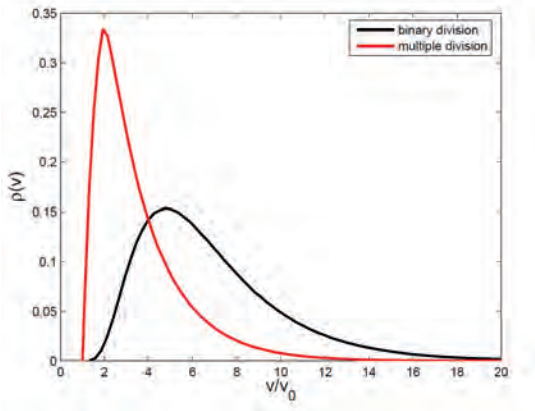

Fig. 2: Probability density for the cell volume under constant light conditions in units of the minimum volume v_0 of a viable cell. The two plots, computed with our model, compare two possible distributions assuming either binary divisions with two daughter cells or multiple divisions with more than two daughter cells as observed for chlamy cells.

Another set of experiments is performed by Martin Steup at the University of Potsdam, in which cells are synchronized by fixed periods of light and darkness. The cells are grown in a special medium that does not allow cell growth in the darkness. Synchronisation relies on the fact that, under certain general conditions, all cells would divide after the start of the dark period and the daughter cells would start to grow only when light is turned on again. By diluting the cells to a fixed density at every start of the light period and by renewing the cultivation medium, it is possible to observe the population over a long period of time under the same set of conditions.

This set-up has the advantage that both the average growth rate of the cells during the light period, the number of cells in the cultivation and, to a certain extent, the number of cell divisions can all be observed simultaneously. Moreover, during these synchronisation experiments, in which both the light and the dark periods typically last twelve hours, one can easily measure the cell size distribution of the cells. Our current aim is to adapt our model to predict the cell size distribution at the beginning of the light period.

Angelo Valleriani, Michael Rading, Reinhard Lipowsky
valleriani@mpikg,mpg.de

Activity Patterns on Networks

The biosphere contains many networks built up from rather different elements such as molecules, cells, or organisms. In spite of their diversity, these networks exhibit universal features and generic properties. The basic elements of each network can be represented by nodes or vertices. Furthermore, any binary relation between these elements can be described by connections or edges between these vertices.

By definition, the degree k of a given vertex is equal to the number of edges connected to it, i.e., to the number of direct neighbors. Large networks containing many vertices can then be characterized by their degree distribution, P(k), which represents the probability that a randomly chosen vertex has degree k. Many biological networks are found to be scale-free in the sense that their degree distribution behaves as

$$P(k) \sim 1/k^{\gamma} \text{ for } k > k_0$$

which defines the scaling exponent γ. Another structural property of networks is their assortativity and dissortativity. Networks are assortative or dissortative if vertices with large degree are primarily connected to other vertices with large or small degree, respectively. Biological networks tend to be dissortative.

Fig. 3: Graphical representation of the neural network of C. Elegans. The vertices correspond to sensor (S), Inter (I), and motor (M) neurons; the edges represent chemical links via synapses and electrical connections via gap junctions. The input signal is received by the S neurons, processed by the I neurons, and eventually transmitted to the M neurons.

In general, the elementary units or vertices of biological networks are dynamic and exhibit various properties or internal degrees of freedom that evolve with time. A more detailed description of the network is then obtained in terms of dynamical variables that are defined for each vertex of the network. Two examples for such dynamical processes are provided by genetic networks that exhibit a changing pattern of active and inactive genes as well as by neural networks that can be characterized by firing and nonfiring neurons. A relatively simple example for a neural network is shown in **Fig. 3** corresponding to the 302 neurons of the worm C. Elegans.

In general, the dynamics of each vertex is determined by the local interactions of this vertex with its neighbours. One instructive example is provided by local majority rule dynamics which is defined as follows: If, at a certain time, most direct neighbors of a certain vertex are active or inactive, this vertex will become active or inactive at the next update of the pattern.

If one starts with a certain pattern of active and inactive vertices, the synchronous update of all vertices according to their local rules determines the time evolution of the activity pattern on the whole network, see **Fig. 4**. For long times, all activity patterns evolve towards one of the attractors (fixed points, limit cycles, etc) of the global dynamics.

Local majority rule dynamics has always two fixed points corresponding to two completely ordered patterns, the all-active pattern and the all-inactive one. In fact, for random scale-free networks without degree-degree correlations, these two fixed points are the only attractors of the dynamics as has been shown in previous studies. **[1]**

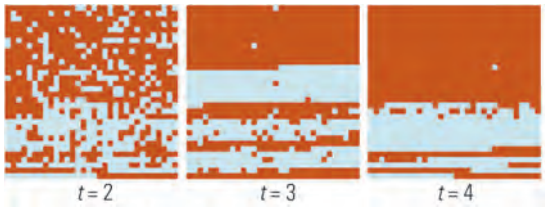

Fig. 4: Time evolution of activity pattern towards an attractor that switches back and forth between the two patterns for t = 3 and t = 4. In each panel, the vertices are arranged according to their degree starting with the smallest degree in the upper left corner and ending with the largest degree in the lower right corner.

This situation changes drastically for majority rule dynamics on scale-free networks with degree correlations. In the latter case, the activity patterns are governed by a large number of attractors. One example corresponding to a limit cycle of period two is displayed in **Fig. 4**. In fact, dissortative scale-free networks have the interesting property that the number of attractors exhibits a maximum as a function of network size. **[2]**

Angelo Valleriani, Jörg Menche, Reinhard Lipowsky
valleriani@mpikg.mpg.de

References:

[1] Zhou, H., and Lipowsky, R.: Activity patterns on random scale-free networks: Global dynamics arising from local majority rules. J. Stat. Mech: Theory and Experiment **2007**, 01009 (2007).

[2] Menche, J., Valleriani, A. and Lipowsky R.: Complex dynamics on dissortative scale-free networks. In preparation.